SIMULIA

3DEXPERIENCE®

XFlow 2022
VALIDATION GUIDE

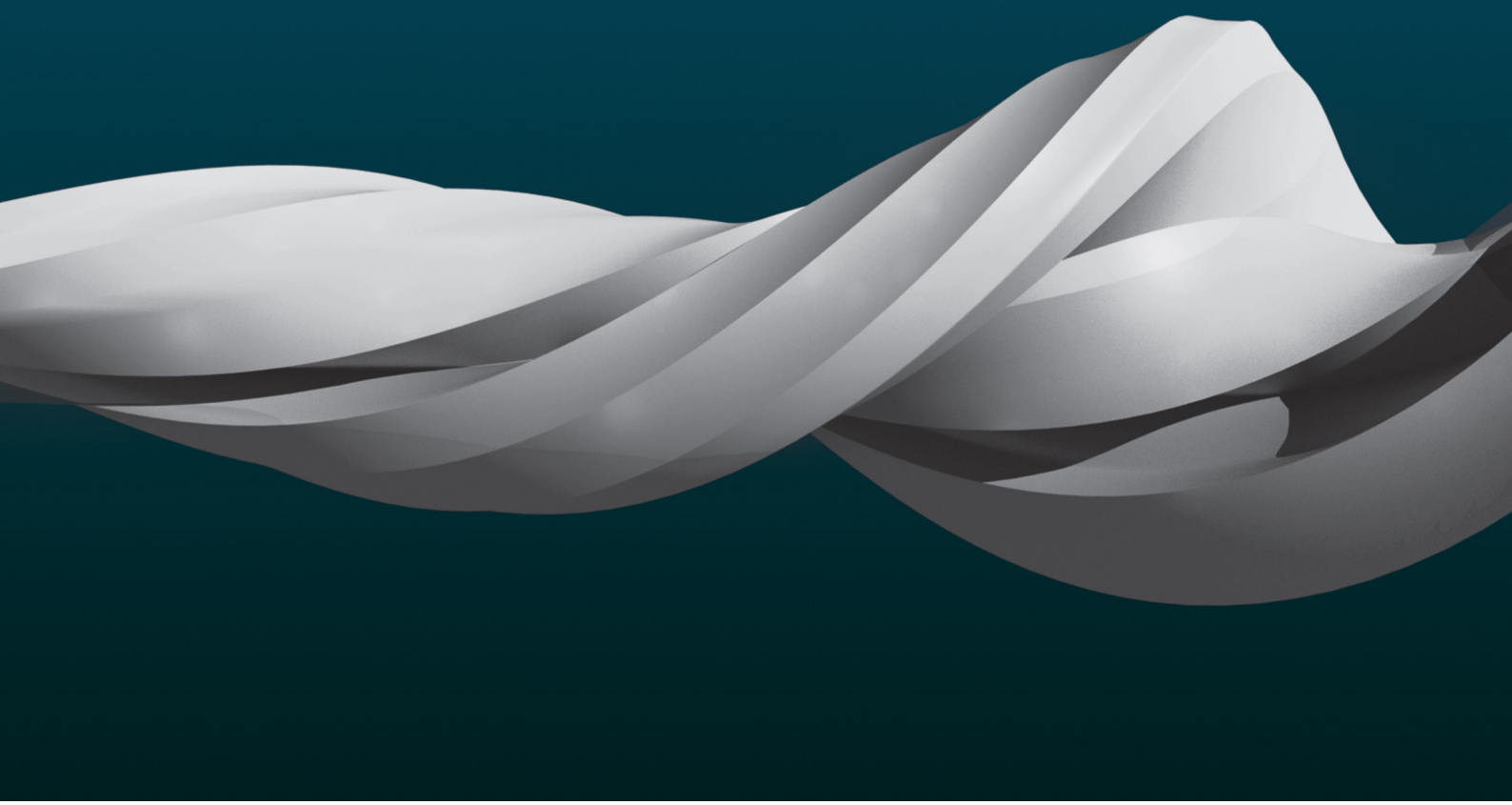

Trademarks

Legal Notices

SIMULIA XFlow is © 2011 - 2021 Dassault Systèmes España, SLU .

XFlow 2022 Validation Guide

Contents

Validation guide

The aim of this guide is to present a set of test cases which show the applicability of *XFlow* in a wide range of applications:

1. Fluid mechanics fundamentals
2. Aerodynamics
3. Automotive
4. Free surface flows
5. Acoustics
6. Heat transfer
7. Multi-phase flows

1 Fundamentals

Contents

1.1 Lid-driven cavity flow

The lid-driven cavity is a classical benchmark problem for viscous incompressible fluid flow. It consists in a cavity where the upper boundary moves to the right, and causes a rotation in the cavity. Side and bottom walls of the cavity are considered no-slip, while the velocity at the upper wall is imposed to $v_x = 1$ m s^{-1} (see Figure 1.1). Although there is a discontinuity of the boundary conditions at the two top corners where the side wall meet the lid, this corner singularity plays a minor role in the overall solution field.

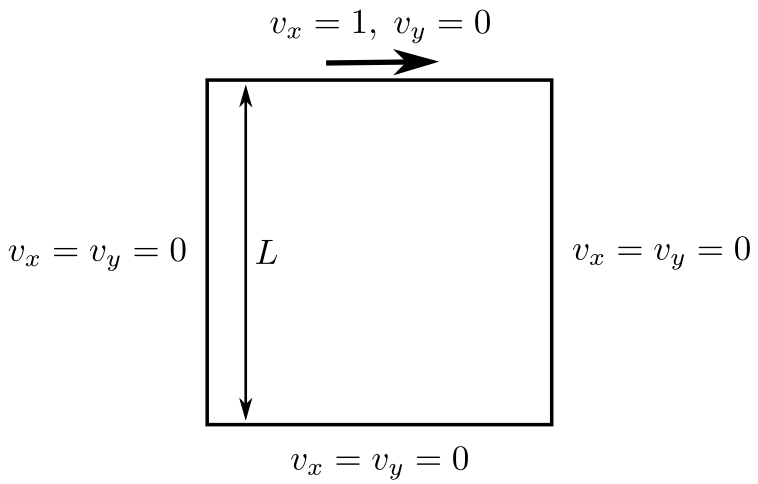

Figure 1.1: Geometry and boundary conditions.

The solution field will depend on the Reynolds number

$$Re = \frac{\rho\, v_x\, L}{\mu} \tag{1.1}$$

This validation case computes the laminar incompressible flow for a 2D driven cavity at $Re = 1000$ and compares *XFlow*'s results with the ones presented in [1]. Fluid properties are $\rho = 1$ kg m^{-3} and $\mu = 0.001$ Pa s, in a $L = 1$ m square cavity discretized with 128x128, 256x256 and 512x512 lattice points.

The case should be set up as an external flow, using a Generic Rectangular Domain, with initialized flow of $v_x = 1$ m s^{-1}, $v_y = 0$ m s^{-1}. The origin of the system should match the center of the doamain. All walls should be resolved with no slip condition, except the top wall which has $v_x = 1$ m s^{-1}. Turbulence should be turned off for this Re, and it is essential to activate the high order boundary conditions: `Environment > Engine > Advanced Options > High order boundary conditions`. This imposes a a high order scheme for the velocity at the lid, which gives a relative error of $\mathcal{O}(10^{-3})$ whereas it is of $\mathcal{O}(10^{-2})$ with the default boundary conditions. With these settings, the flow field will become stabilized after 50s of simulated time.

The velocity field computed with *XFlow* is plotted in Figure 1.2. The v_x velocity distribution along vertical centerline is shown in Figure 1.3 and Table 1.1. In order to obtain the displayed results, it is suggested to create plot lines with extremes located at the voxel of the lattice elements adjacent to the walls, and a number of points equal to the lattice resolution (128, 256, 512). For example, for the 128x128 resolution, the plot line should have the following settings:

$Vertex_1$ = (0, -0.4961, 0)

$Vertex_2$ = (0, 0.4961, 0)

Number of points =128

y	128x128	256x256	512x512	Ref. [2]	Ref. [1]
0.9688	0.57874	0.58261	0.58212	0.57492	0.58031
0.9531	0.47825	0.47344	0.47341	0.46604	0.47239
0.7344	0.19412	0.19016	0.19013	0.18719	0.18861
0.5	-0.06265	-0.06174	-0.06209	-0.0608	-0.06205
0.2813	-0.28269	-0.27995	-0.28073	-0.27805	-0.2804
0.1016	-0.30371	-0.30217	-0.30168	-0.2973	-0.30029
0.0625	-0.20525	-0.20415	-0.20344	-0.20196	-0.20227

Table 1.1: Horizontal velocity v_x along the vertical centreline. Comparison of *XFlow*'s results for different resolutions with the reference solutions.

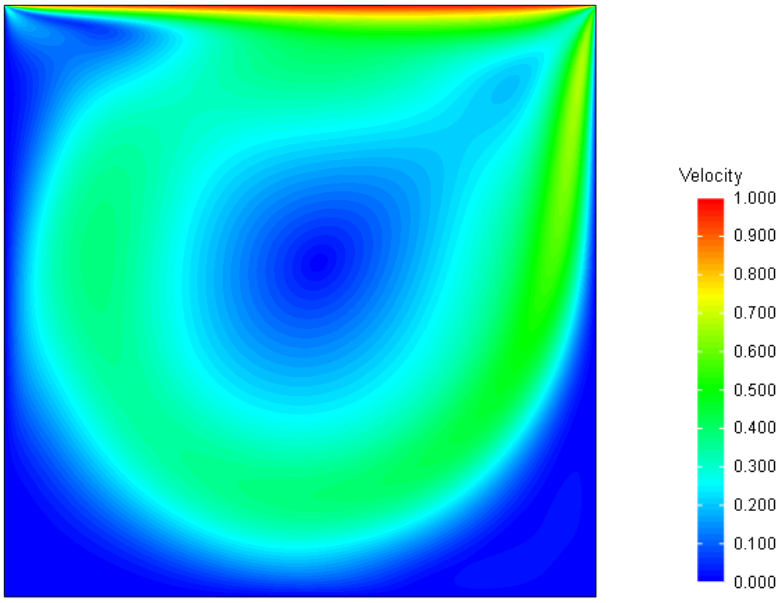

Figure 1.2: Velocity field.

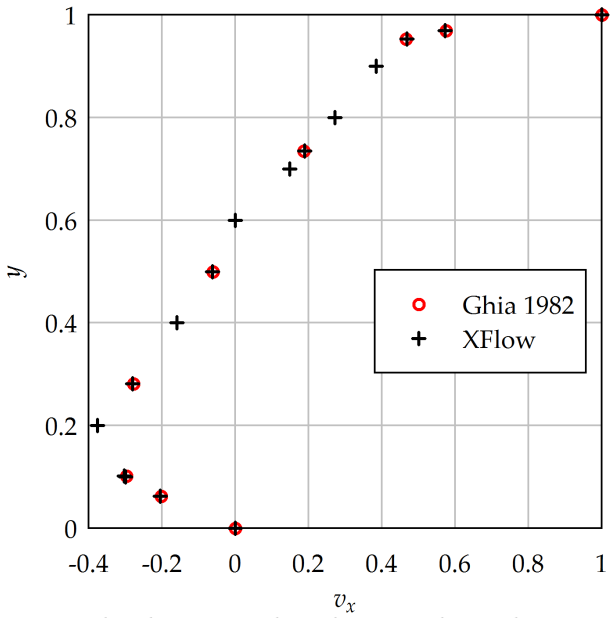

Figure 1.3: Horizontal velocity v_x distribution along the vertical centreline.

Additional quantitative comparisons of pressure and vorticity are presented in Tables 1.2 and 1.3.

y	128x128	256x256	512x512	Ref. [2]
0.9688	0.05388	0.05264	0.05207	0.051514
0.9531	0.05275	0.05150	0.05091	0.050329
0.7344	0.01396	0.01304	0.01259	0.012122
0.5	0.0	0.0	0.0	0.0
0.2813	0.04064	0.04043	0.04038	0.040377
0.1016	0.10581	0.10490	0.10452	0.104187
0.0625	0.11148	0.11026	0.10972	0.109200

Table 1.2: Pressure p along the vertical centreline for $Re = 1000$. Comparison of *XFlow*'s results for different resolutions with a reference solution.

y	128x128	256x256	512x512	Ref. [1]
0.9688	11.907	11.26092	10.9246	9.47810
0.9531	6.66407	5.97346	5.68313	4.86280
0.7344	2.35950	2.34076	2.33212	2.09090
0.5	2.35591	2.32528	2.31102	2.06690
0.2813	2.49017	2.50176	2.50973	2.26780
0.1016	1.68321	1.74846	1.78189	-1.63520
0.0625	2.52116	2.54815	2.56153	-2.31740

Table 1.3: Vorticity ω along the vertical centreline. Comparison of *XFlow*'s results for different resolutions with a reference solution.

1.2 Taylor Green vortex

Taylor Green vortex a is three dimensional periodic, transitional and incompressible flow which one can study the generation of small scales by three-dimensional vortex stretching and the resulting turbulence. This process controls the turbulent-energy dynamics and therefore the global structure and evolution of the flow.

The computation domain is a periodic cube defined as $-\pi L \leq x, y, z \leq \pi L$, with a reference length $L = 1$ m. The fluid properties are $\rho_0 = 1$ kg m^{-3}, $p_0 = 0$ Pa, $V_0 = 1$ m/s, $\mu = 0.000625$ Pa.s and the initial conditions (see Figure 1.4) for this flow evolution is given by:

$$u_x = V_0 sin(\frac{x}{L})cos(\frac{y}{L})cos(\frac{z}{L}) \tag{1.2a}$$

$$u_y = -V_0 cos(\frac{x}{L})sin(\frac{y}{L})cos(\frac{z}{L}) \tag{1.2b}$$

$$u_z = 0 \tag{1.2c}$$

$$p = p_0 + \frac{\rho_0 v_0^2}{16}(cos(\frac{2x}{L}) + cos(\frac{2y}{L}))(cos(\frac{2z}{L}) + 2) \tag{1.2d}$$

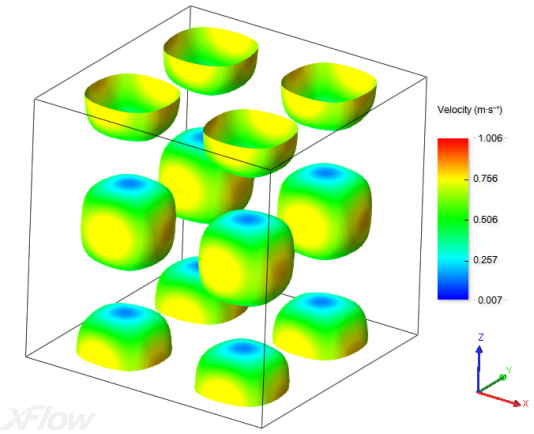

Figure 1.4: Taylor Green vortex initial condition: isosurface of vorticity coloured by the velocity field

The solution field will depend on the Reynolds number:

$$Re = \frac{\rho_0 V_0 L}{\mu} \tag{1.3}$$

This validation case computes the incompressible flow at $Re = 1600$ and compares *XFlow*'s results with the ones provided by the Université Catholique de Louvain [3] using a dealiased pseudo-spectral code for which neither numerical dissipation nor numerical dispersion errors occur. The domain has discretized with $64 \times 64 \times 64$,

$128 \times 128 \times 128$ and $256 \times 256 \times 256$ lattice elements in order to check the grid convergence.

The goal of this validation case is to compare the kinetic energy dissipation rate $\epsilon = \frac{dE_k}{dt}$ and the energy spectrum function $E(k)$ with the spectral data .

The kinetic energy dissipation rate is the energy dissipated due to the work done by the fluctuating viscous stresses in resisting deformation of the fluid material by the fluctuating strain rates. *XFlow* allows to export directly the kinetic energy (E_k) integrated over the whole volume (Ω) from the Function viewer (Other integrals > Overall kinetic energy):

$$E_k = \frac{1}{\rho_0, \Omega} \int_{\Omega} \rho \frac{v \cdot v}{2} d\Omega \tag{1.4}$$

Then, the kinetic energy dissipation rate is calculated by the time derivation of this kinetic energy provided by *XFlow*.

All the grid configurations have been simulated with the same time step $dt = 0.001$ s. In the Figure 1.5, it can be seen that, increasing the refinement, the turbulence dissipation gets closer to the spectral data. It has been calculated with a central finite difference as numerical approximation of the derivate ($\epsilon = \frac{dE_k}{dt}$) .

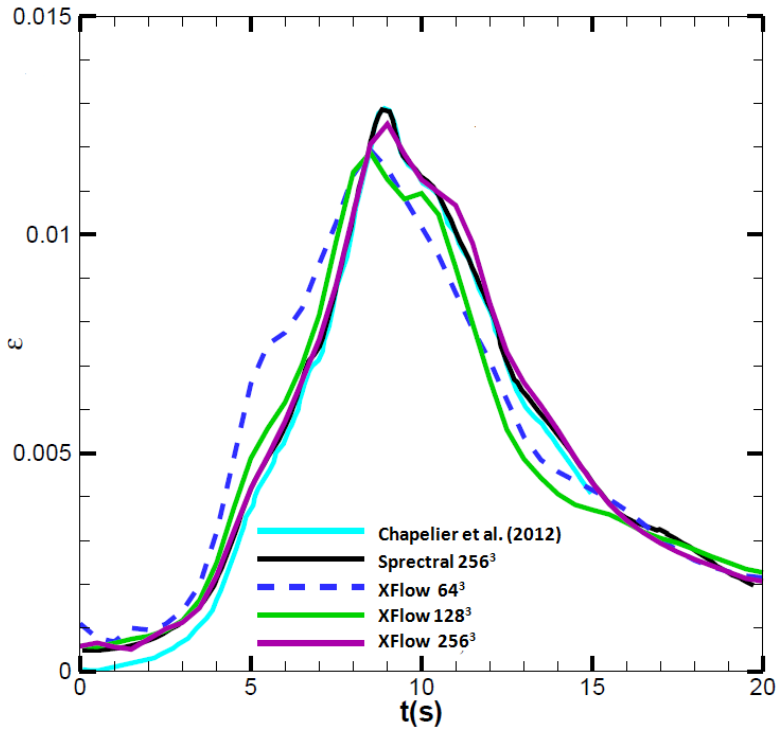

Figure 1.5: Energy dissipation rate in function of time at different resolutions

The energy spectrum function E(k) is a characterization of the turbulent flow in a case of homogeneous turbulence. The magnitude k is the modulus of the wavevector which corresponds to some harmonics in a Fourier representation of the flow velocity field $u(x)$. This $u(x)$ is defined as it follows:

$$u(x) = \iiint \hat{u}(k) e^{i\bar{k}\bar{x}} d^3k \tag{1.5}$$

where $\hat{u}(k)$ is the Fourier transform of the flow velocity field. The total kinetic energy is calculated as

$$TKE = \int_0^\infty E(k)dk \tag{1.6}$$

Using dimensional analysis, the energy spectrum function according with the third Kolmogorov's hypothesis is:

$$E(k) = C\varepsilon^{2/3}k^{-5/3} \tag{1.7}$$

In order to compare the theoretical result with the decay of the energy in the simulations, it is necessary to compute the Fast Fourier Transform and consequently, the vector $\bar{k} = (k_x, k_y, k_z)$ is calculated in the three directions of the space. The plot is carried out taking into account the contribution to the kinetic energy of the three components of the velocity and the wavelength is calculated as: $k = \sqrt{k_x^2 + k_y^2 + k_z^2}$. These results are plotted in the following figure:

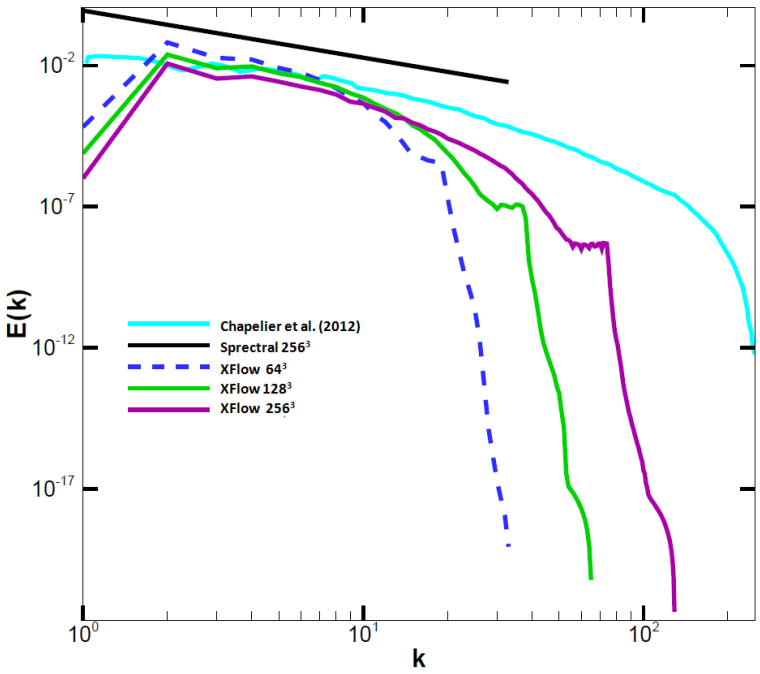

Figure 1.6: Total Kinetic Energy spectra

As it can be appreciated in the Figure 1.6, the decay of the kinetic energy is produced for higher wavelengths when the lattice length unit is reduced. Indeed, at larges wavenumber or smaller sizes, as the lattice length is reduced, the mesh is able to capture smaller eddies and, consequently, there are more eddies . Besides this, the Figure 1.6 suggests that the decay of the kinetic energy in the short wavelength is similar to the slope $k^{5/3}$, but, instead, in the smallest scales the simulations have bigger decay, which relates to the LES filter.

Finally, the volumetric isosurface computed at $t = 20$ s with *XFlow* is plotted in Figure 1.7.

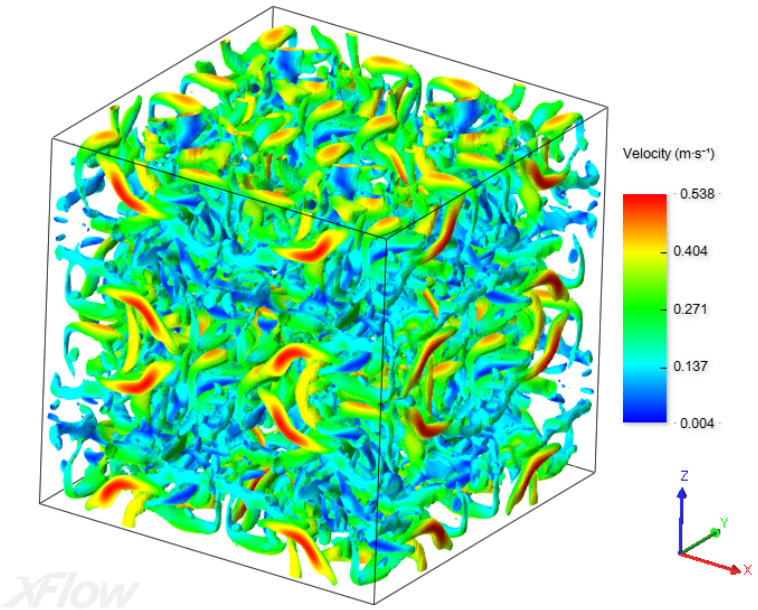

Figure 1.7: Isosurface of vorticity with 256^3 elements and $dt = 0.001$ s at $t = 20$ s

2

Aerodynamics

Contents

2.1 NACA-0012 airfoil at Re = 500

The NACA-0012 airfoil is a widely-used wing section that has zero camber and a maximum thickness to chord ratio of 12 percent. As it is shown in Figure 2.1, the NACA-0012 is a symmetric two-dimensional profile with a very smooth aerodynamic shape.

This validation case presents the *XFlow* results for the flow past a NACA-0012 at zero angle-of-attack and at a Reynolds number of 500. These results are further compared with reference data; the comparison is based on the CFL3D code from the National Aeronautics and Space Administration (NASA)[1] [4, 5] due to the lack of experimental data for such a low Reynolds number. A two-dimensional single phase

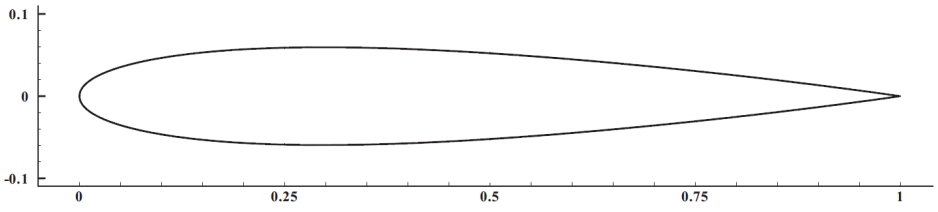

Figure 2.1: NACA-0012 profile.

[1] Acknowledgements: Validation data have been kindly provided by courtesy of NASA Langley Research Center and David P. Lockard.

external aerodynamics analysis has been performed using a virtual wind tunnel of dimensions 60×40 m and a NACA-0012 profile of chord length $L = 1$ m. In order to reach a Reynolds number based on the chord length equal to 500, the simulation parameters have been set according to Table 2.1. As shown in Figure 2.2, the

Free-stream velocity	v_{ref}	50 m s^{-1}
Density	ρ	1 kg m^{-3}
Dynamic viscosity	μ	0.1 Pa s
Chord length	L	1 m
Reynolds number	Re	500
Angle-of-attack	α	0 degree

Table 2.1: Simulation conditions.

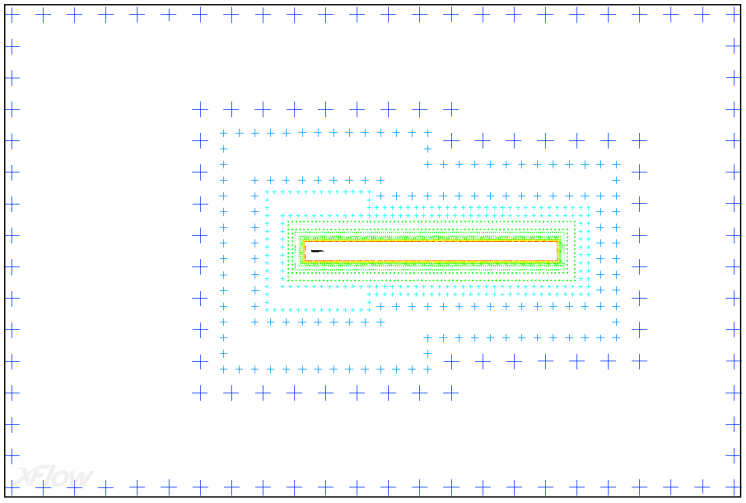

Figure 2.2: Spatial resolution in *XFlow*.

spatial resolution is 2.56 m for the far field, and 0.005 m around the airfoil profile and within the wake area. The spatial discretization has been defined through a region of refinement instead of using an adaptive refinement in order to ensure that the symmetry of the NACA-0012 is respected. The discretization ended up with 1.3 million elements in 9 levels of refinement. Since the flow is laminar, no wall functions have been used to model the boundary layer.

Regarding temporal discretization, the time step was set to 0.004 s, which corresponds to a Courant number of 1 with respect to the lattice size and the free-stream velocity. Due to the fact that *XFlow* solver is inherently transient and this case is steady, the analysis has been run until the aerodynamic coefficients stabilize in time. The values of these coefficients are given in Table 2.2; the ones predicted by *XFlow* are quite similar to those from CFL3D. The drag coefficient (C_d) has a relative error of -2.0678% with respect to CFL3D results, whereas the lift coefficient(C_l)

is actually even more accurate as it should theoretically be theoretically equal to zero because of the NACA symmetry at zero angle-of-attack. XFlow profiles of

	XFlow	CFL3D	Objective
C_d	0.173	0.1741	0.1741
C_l	10^{-15}	-0.538×10^{-5}	0

Table 2.2: Aerodynamic coefficients comparison.

normalized X and Y velocity components as well as pressure coefficients have been compared with CFL3D data at five vertical sections: $x/L = 0$, 0.25, 0.5, 0.75 and 1 (see Figure 2.3). Figure 2.4 shows the X-component of the velocity field normalized

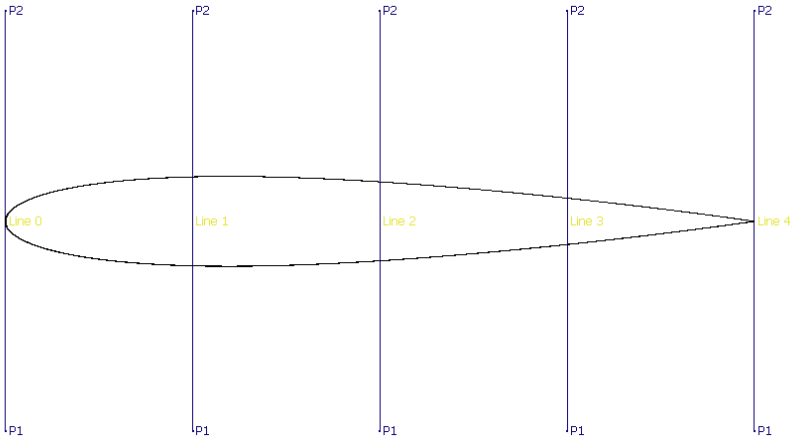

Figure 2.3: Data plot lines.

by the reference velocity $v_{ref} = 50$ m s^{-1}. The results of XFlow and CFL3D are perfectly matching for the five sections. The profiles are as expected in both codes: they tend to zero in the airfoil thickness and to one (or slightly more) on the sides where the boundary layer is fully developed. For the Y-component of the velocity field (normalized by v_{ref}), again XFlow results are almost perfectly matching with those of CFL3D, as shown in Figure 2.5. Nevertheless, one can observe some differences close to the airfoil wall, specially for section $x/L = 0.5$. This might be due to the size of the first element within the boundary layer which is not fine enough. However, the differences between the two codes are small. The pressure coefficient C_p is defined as $C_p = \dfrac{p_{static}}{\frac{1}{2}\,\rho\, v_{ref}^2}$, where p_{static} is the gauge static pressure. Figure 2.6 shows the pressure coefficient distribution at the five sections. More differences are now noticeable, especially at $x/L = 0.5$, 0.75 and 1.0. In general, the C_p tends to be slightly over-estimated.

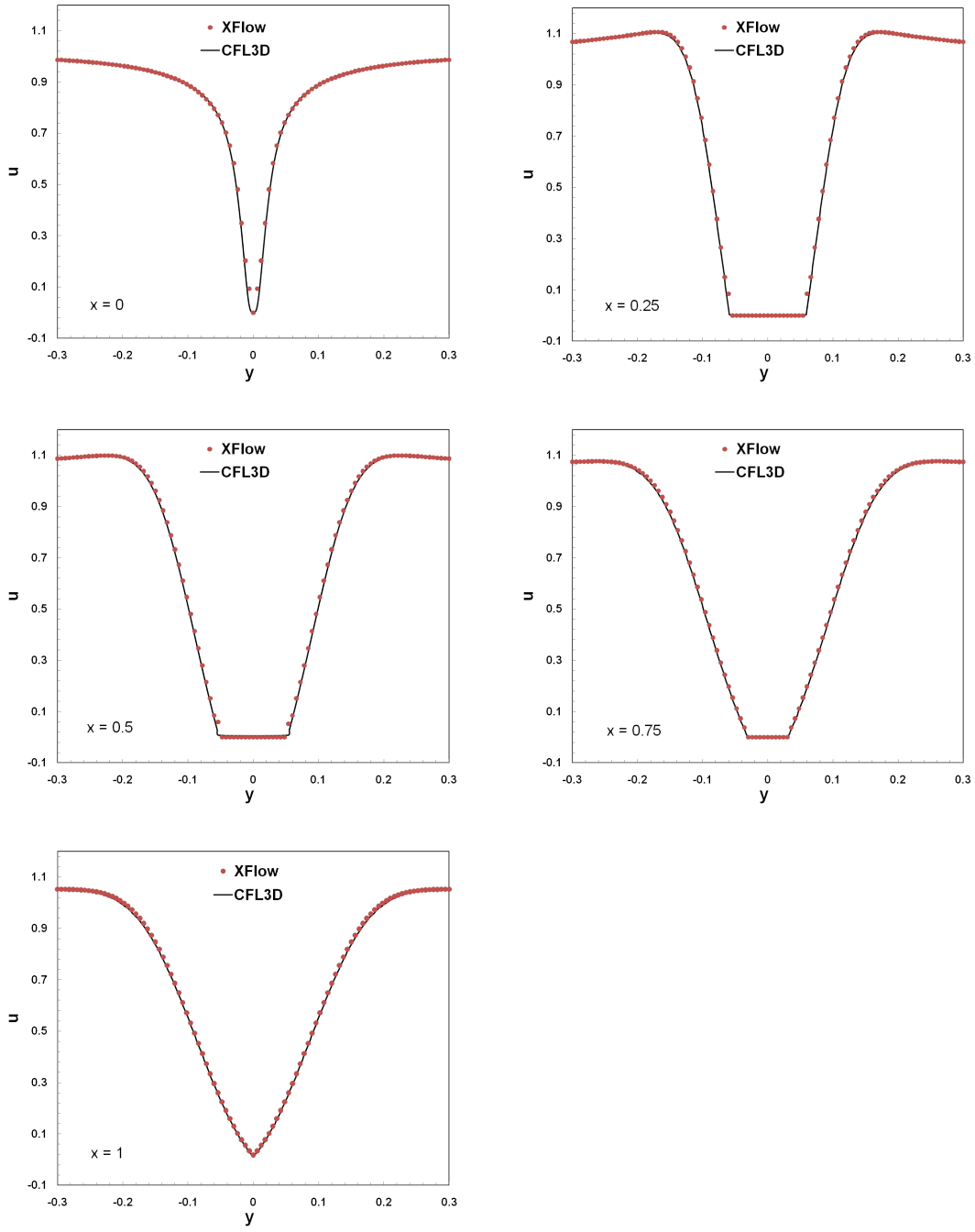

Figure 2.4: X-component of velocity $u(x, y)$ at $x/L = 0.0$, 0.25, 0.50, 0.75 and 1.0.

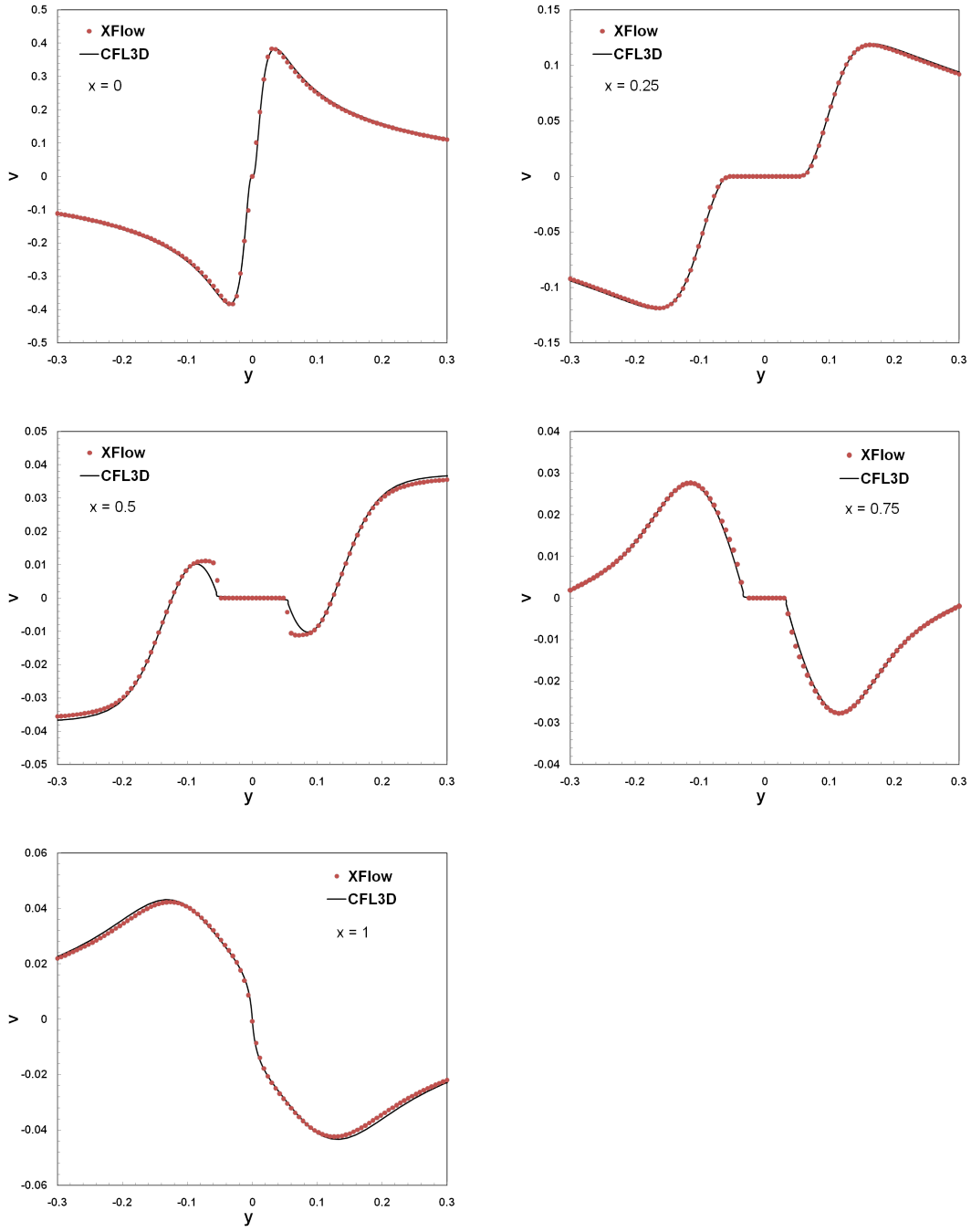

Figure 2.5: Y-component of velocity $v(x, y)$ at $x/L = 0.0$, 0.25, 0.50, 0.75 and 1.0.

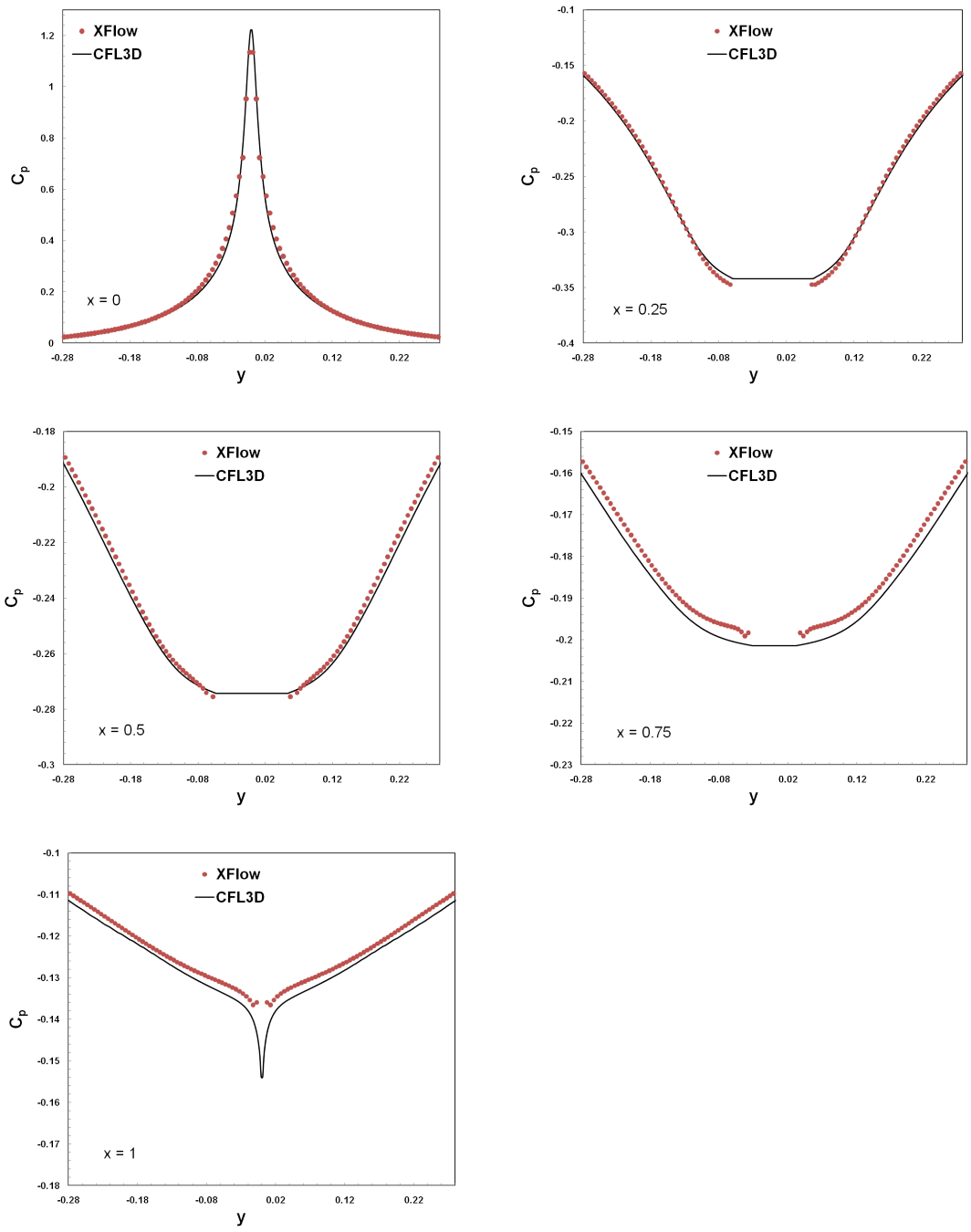

Figure 2.6: Pressure coefficient at $x/L = 0.0$, 0.25, 0.5, 0.75 and 1.0.

2.2 S825 airfoil

The S825 airfoil has been designed for horizontal-axis wind turbine applications by the National Renewable Energy Laboratory (Colorado, USA). The report of the design and experimentation of the S825 airfoil [6] exposes the different objectives and constraints set for the design, as well as the methodology of measurements which have been conducted in the NASA Langley Low-Turbulence Pressure Tunnel (LTPT) [7]. As explained in [6], the main objectives were, first, to reach a maximum lift coefficient of at least 1.40 at a Reynolds number of 2×10^6. Second, a low profile-drag coefficients should be obtained between 0.40 and 1.20 of the lift coefficient. Two main constraints were to keep the zero-lift pitching-moment coefficient greater than -0.15, and also to have an airfoil thickness equal to 17% of the chord. The final two-dimensional design is as shown in Figure 2.7, with a chord length equal to 0.45715 m.

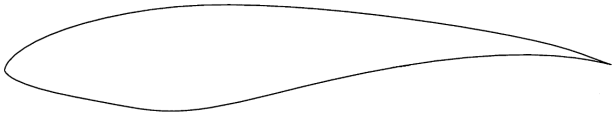

Figure 2.7: S825 airfoil shape.

Experiments have been conducted at different Reynolds numbers based on the chord length, however this validation case will only treat the Reynolds number 2×10^6 since it has been used for most of the data provided by [6]. The Mach number is 0.1 and the experimentation has been done with transition free (smooth) and with transition fixed by roughness at specific locations.

The objective of this case is to validate the pressure distribution and aerodynamic forces predicted by *XFlow* at low Mach number and different angles of attack (AoA).

The calculations have been performed with *XFlow* for a range of angles of attack between -4 and 10 degrees every two degrees. All the calculations are transient due to the nature of the *XFlow* solver and use the Wall-Adapting Local-Eddy turbulence model, which belongs to the Large Eddy Simulation (LES) approach. Wall function models in *XFlow* assume that the boundary layer is fully turbulent, therefore it is not possible to model transition or prescribe a transition location.

Two-dimensional single phase analyses have been performed using a virtual wind tunnel of 60 m $\times$ 40 m and a velocity at the inlet of 43.7493 m s^{-1}. The angle of attack is varying by rotating the geometry instead of projecting the inlet velocity vector, since *XFlow* allows easy manipulation of the geometry.

The fluid has a density of 1 kg m^{-3} and a dynamic viscosity of 10^{-5} Pa s accordingly

to the Reynolds number based on the airfoil chord length ($Re = 2 \times 10^6$). The simulations have been run for 1 second of physical time, with a time step of 0.002 s. The resolution scale at the far field is 1.28 m, using the adaptive refinement algorithm available in *XFlow*. The walls and the wake are resolved with a scale of 0.0025 m, as shown in Figure 2.8.

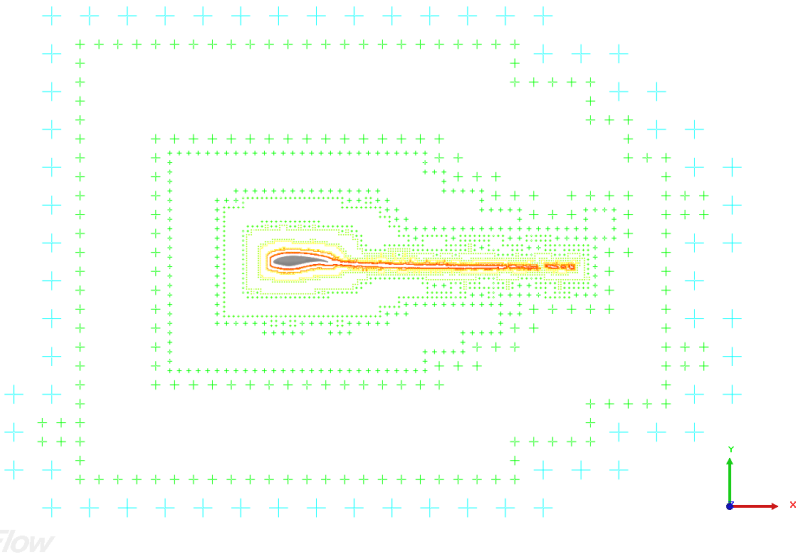

Figure 2.8: Resolution refinement near the airfoil and the wake.

The solution for the static pressure and velocity flow variables at final time for zero angle of attack can be observed in Figure 2.9.

For each angle of attack, the curve of pressure coefficients (C_p) has been extracted in *XFlow* using a cutting plane field distribution which projects the selected field on the upper and lower sides of the airfoil. The C_p has been computed as following, being V_{ref} equal to 43.7493 m s^{-1}:

$$C_p = \frac{p_{static}}{\frac{1}{2}\,\rho\,V_{ref}^2} \tag{2.1}$$

For the angles of attack -4, -2, 0, 2, 4, 6, 8 and 10 degrees, the pressure coefficient distribution along the airfoil has been compared with the transition free experimental data presented in [6]. The results for angle of attack between 0 and 6 degrees are in good agreement with the experiments, as shows Figure 2.10. On the upper side of the airfoil, the pressure coefficients are slightly under-estimated when the angle increases but still match reasonably with the experimental data.

However, when angles are increased to 8 and 10 degrees of AoA then results are getting less accurate, as shown in Figure 2.11. The pressure coefficient tends to be more under-estimated near the leading edge of the upper part. This could be

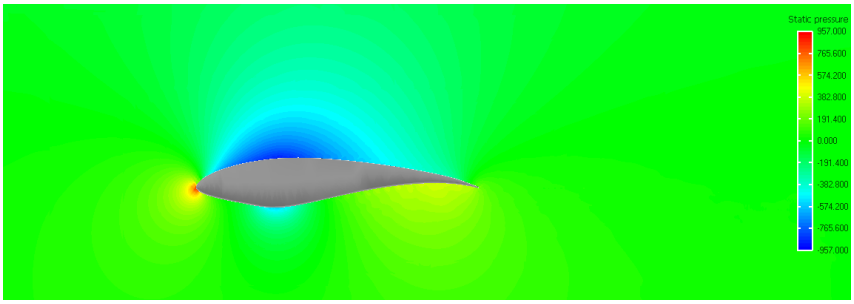

(a) Static pressure

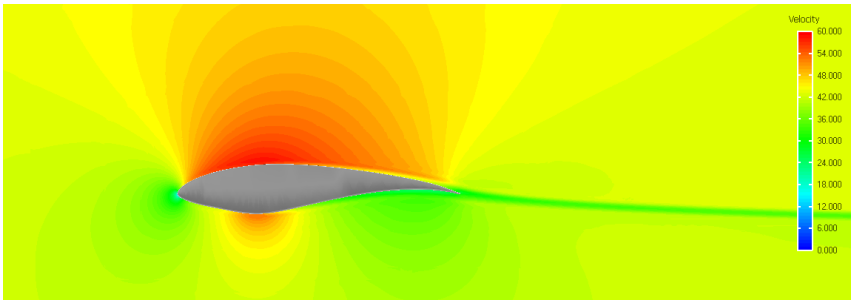

(b) Velocity

Figure 2.9: Static pressure and velocity flow fields at final time for AoA = 0 degrees.

explained by the lack of transition model or the LES model, which is not fully consistent for 2D simulations.

Another last series of angles of attack have been studied, this time for negative incidence. Again, *XFlow* predicts with accuracy the pressure coefficient distribution for -2 and -4 degrees, as shown in Figure 2.12.

Finally, Figure 2.13 compares the angle of attack vs. lift coefficient for theoretical [6], experimental [6] and *XFlow* results. For positive angles, the lift coefficient is slightly over-predicted by *XFlow* but in good agreement with the theoretical results.

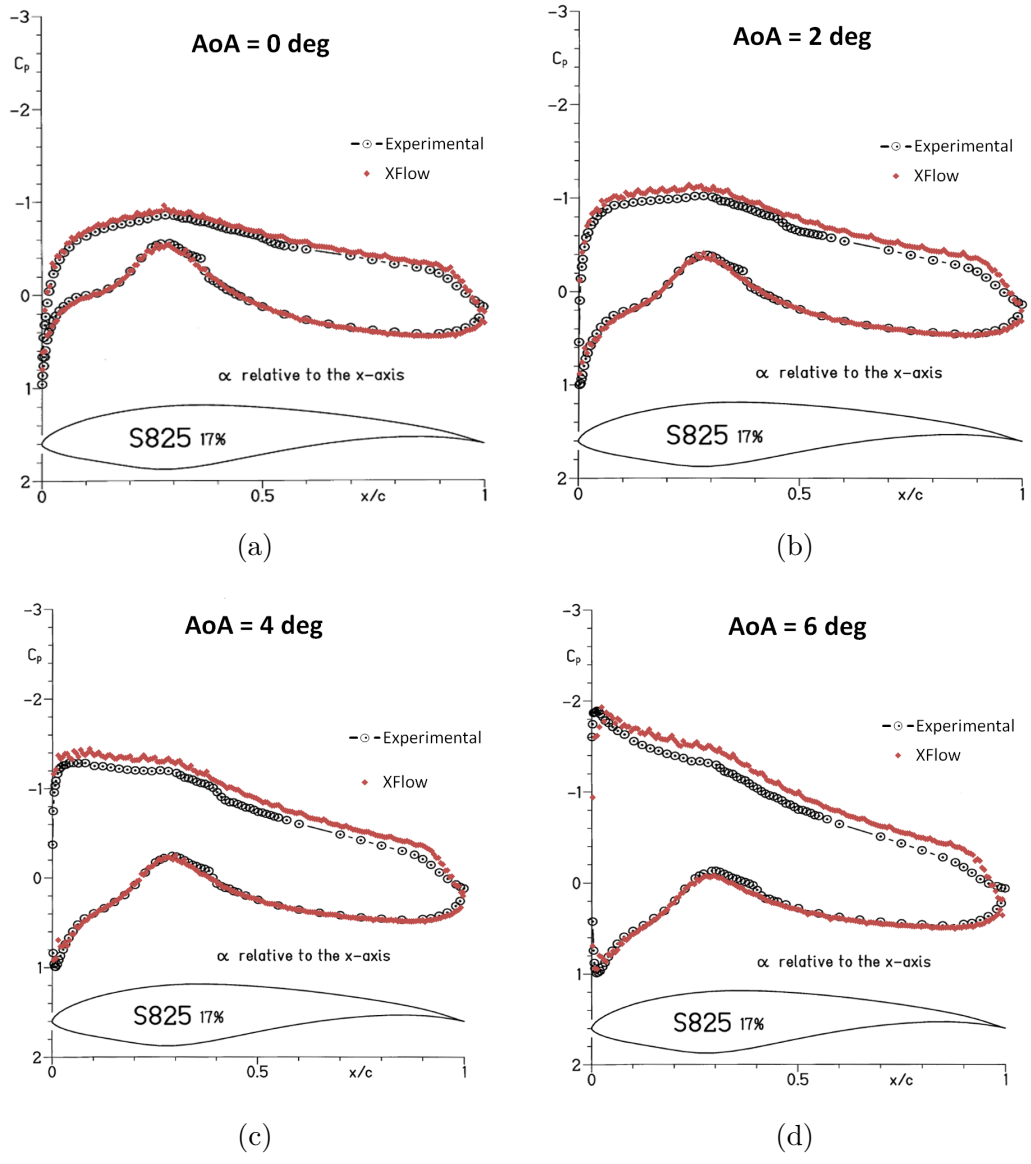

Figure 2.10: Airfoil pressure coefficient distribution for different AoA: a) 0 degrees, b) 2 degrees, c) 4 degrees, d) 6 degrees.

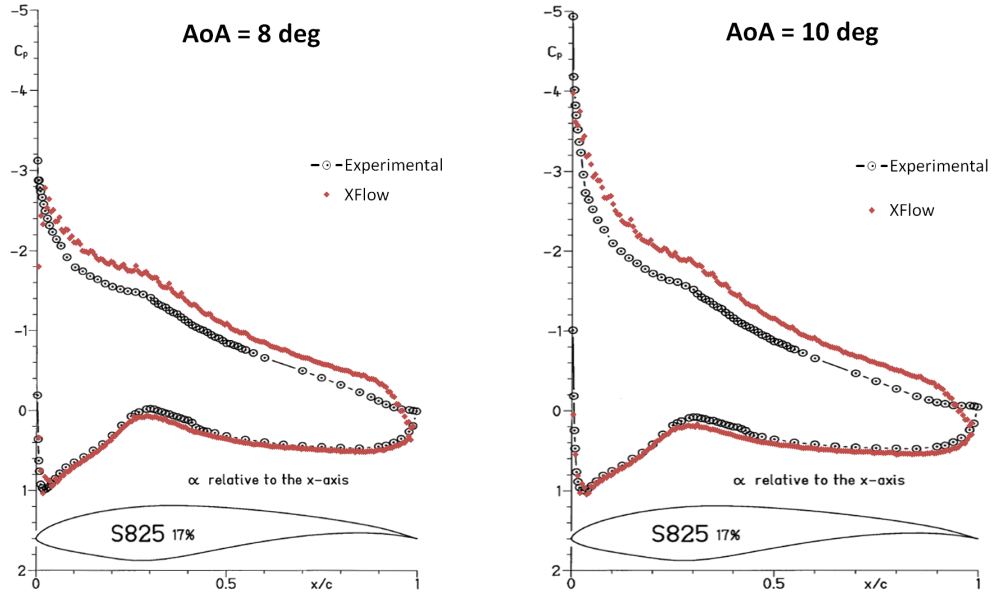

(a) (b)

Figure 2.11: Airfoil pressure coefficient distribution for different AoA: a) 8 degrees, b) 10 degrees.

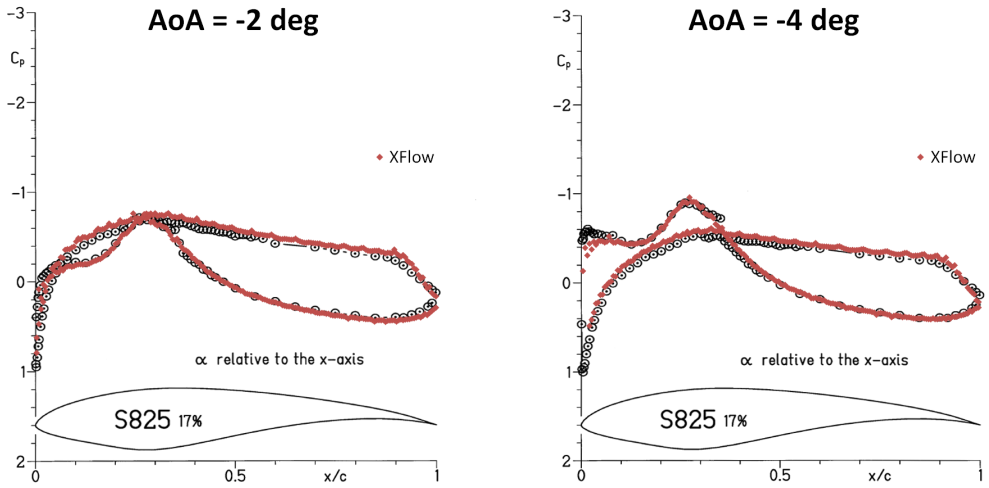

(a) (b)

Figure 2.12: Airfoil pressure coefficient distribution for different AoA: a) -2 degrees, b) -4 degrees.

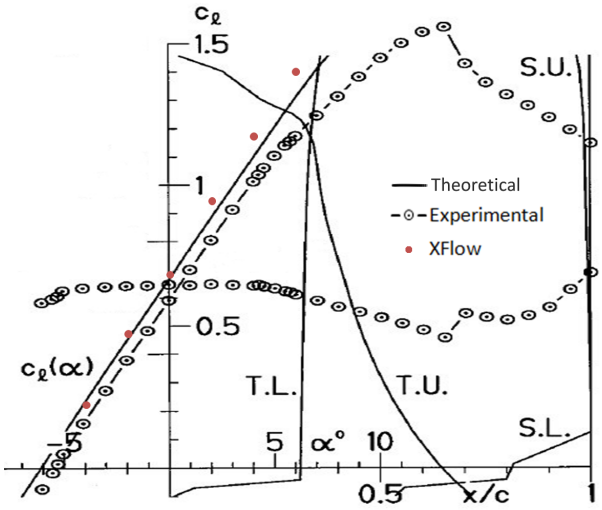

Figure 2.13: AoA (α) vs. lift coefficient (C_l) for theoretical, experimental and *XFlow* results, adapted from [6]

2.3 Vortex cell

Trapping vortices is a technique that prevents vortex shedding in flows past bluff bodies. Vortices forming near bluff bodies tend to be shed downstream but, if the vortex is kept near the body at all times, it is called trapped.

This validation case compares *XFlow* results with experimental data for the flow inside a vortex trapping cavity (vortex cell). The geometry consists in a rectangular channel of section 520×52 mm with a spherical vortex cell of 45 mm depth located at mid-length as shown in Figure 2.14. The boundary condition at the inlet is set to a constant fluid velocity of $U_L = 36$ m/s and the gauge pressure to 0 Pa at the outlet. The fluid has been initialized to U_L in the whole domain except inside the vortex cell where it is 0 m/s in order to reach quicker the pseudo-steady state.

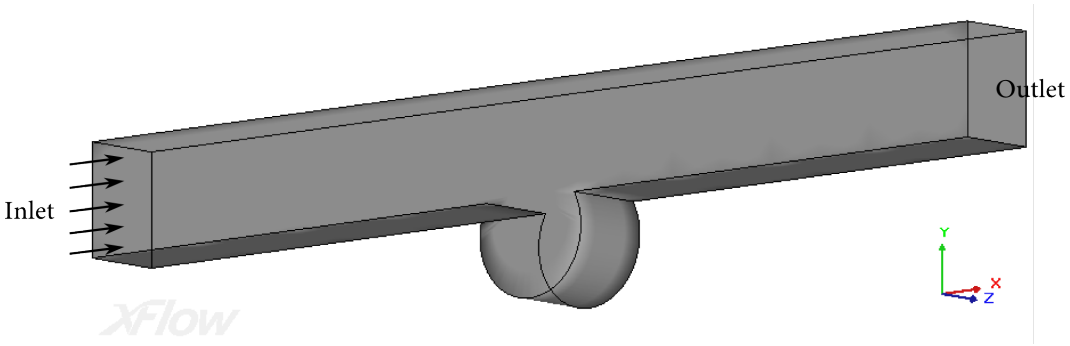

Figure 2.14: Vortex cell geometry.

The experimental data from [8, 9] provide the normalized X-component of the velocity measured along a vertical line going from the bottom of the sphere up to the upper wall of the channel (see Figure 2.15). The vertical coordinate along the line is normalized by the line length $L = 52$ mm.

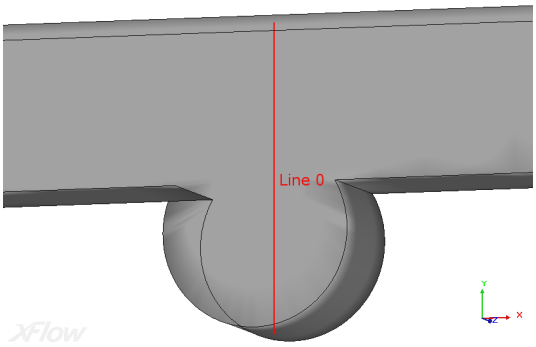

Figure 2.15: Line for measurement.

The two-dimensional studies led by [10] based on steady RANS turbulence models show how sensitive are the numerical results for the vortex cell flow depending

on the turbulence model and the choice of the numerical scheme. XFlow uses Large Eddy Simulation turbulence models, which are inherently three-dimensional. Furthermore, although the vortex cell seems a two-dimensional flow, turbulence effects (important near and inside the cavity) need a three-dimensional analysis to be accurately modeled.

Unfortunately three-dimensional analyses may involve a large number of elements and long simulation times. The refinement algorithms available in XFlow (near the walls and adaptive wake) allow to minimize the number of elements, but tend to introduce numerical dissipation when passing from one element size to another and has been found to be inaccurate especially in the boundary layer that detaches from the leading edge of the vortex cell.

The following results were obtained using a uniform resolution of 1 mm in the whole domain and a time step of 10^{-6} s. This resolution leads to a total of 1.1 million elements. The total simulation time solved is 0.9 s at a frequency of 500 Hz. Averaged results are required in order to analyse the pseudo-steady state of the solution.

Figure 2.16 shows that XFlow 3D results are globally in good agreement with the experimental data. The areas of less accuracy are at y/L around -0.7 and the peak around 0.1. Nevertheless XFlow is able to predict the experimental velocity profile at the cavity entry ($-0.4 < y/L < 0$) better than the RANS calculations and correctly predicts the vortex speed at $y/L = -0.8$.

Finally, Figure 2.17 shows the averaged velocity field computed by XFlow. It is possible to observe the creation of vortices at the leading edge of the cavity, what is not evident in steady calculations.

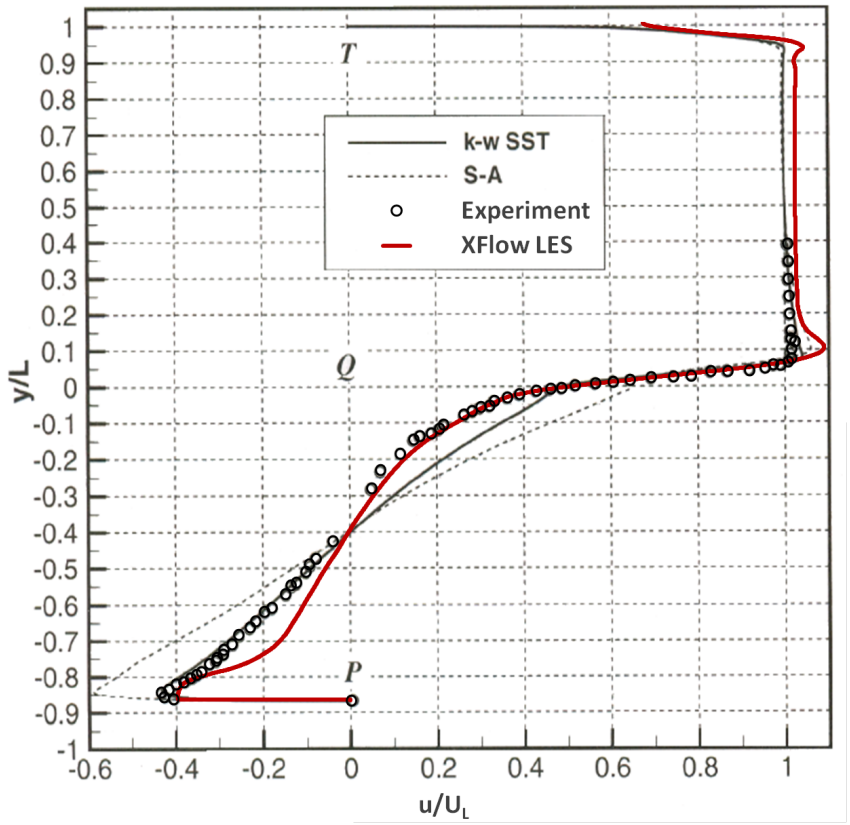

Figure 2.16: Comparison of *XFlow* 3D results with experimental data and RANS results from [10].

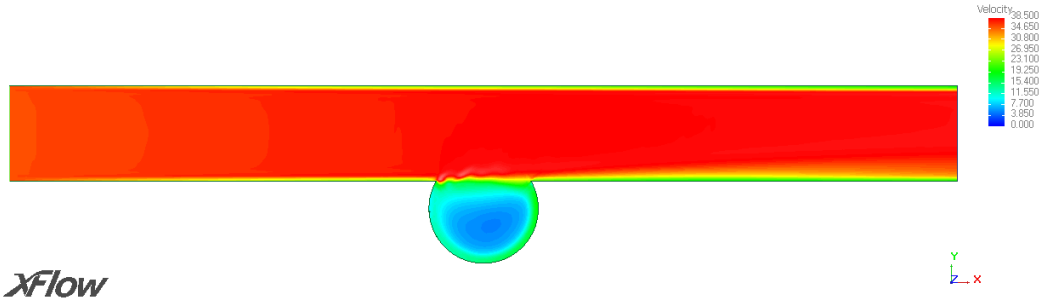

Figure 2.17: *XFlow* averaged velocity field.

2.4 1st AIAA High Lift Prediction Workshop

The 1st AIAA CFD High Lift Prediction Workshop (HiLiftPW-1), took place in June 2010 in Chicago (USA). The challenge was to simulate a half aircraft configuration composed of a body and a 3-element airfoil with a plane of symmetry (as shown in Figure 2.18) for a range of high angles of attack.

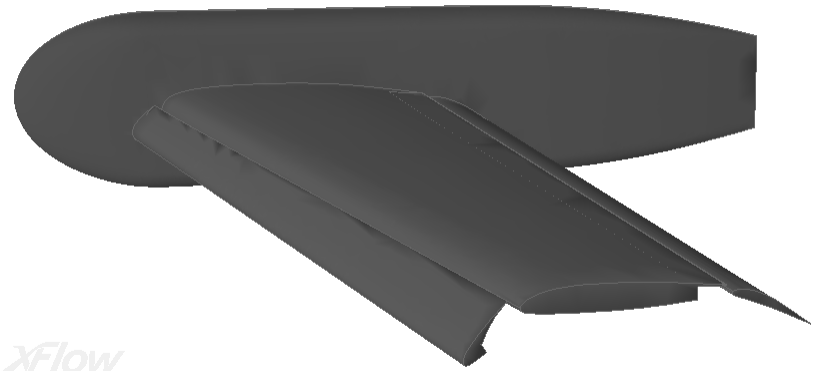

Figure 2.18: Trapezoidal wing, configuration 1.

This validation case reports the results obtained with *XFlow* for the Test Case 1 of the High Lift Prediction Workshop [11]:

- Trapezoidal wing Config 1 (slat at 30 degrees, flap at 25 degrees)
- Mach number = 0.2
- Reynolds number = 4.3E+6 based on mean aerodynamic chord (MAC)
- Geometry provided by the workshop
- MAC = 1.0067 m
- No brackets
- Angles-of-attack: -4, 0, 6, 13, 21, 25, 28, 32, 34 and 37 degrees.

Two different spatial resolutions have been used depending on the lift level, see Table 2.3 for further details.

	Walls	Wake	Far Field	Max # of Particles
Resolution 1	0.005 m	0.01 m	1.28 m	25E+6
Resolution 2	0.005 m	0.02 m	1.28 m	10 E+6

Table 2.3: Spatial discretization.

As it is shown in Figure 2.19, Resolution 1 leads to very large number of elements at high angles-of-attack, which could not be computed with our resources (an Intel quad-core workstation with 16 GB of RAM). This is due to a large number of elements generated for the wake refinement as separation starts to occur and detached eddies leave the airfoil. For this reason Resolution 2, with a coarser refinement for the wake, has been used for the angles-of-attack 34 and 37 degrees (where stall starts to happen) and Resolution 1 for the other angles.

Workshop attendants were asked to run all the simulation as free air (no wind-tunnel walls or model support systems are to be included) and fully turbulent. Since there is a symmetry axis on the geometry model, the airfoil has been placed in the *XFlow* virtual wind tunnel with the ground wall enabled as a free-slip wall, which has been used as the plane of symmetry.

The experimental data have been gathered at the 14x22 wind-tunnel at NASA Langley Research Center [12]. Forces, moments, and C_p distributions have been provided for free transition and with lower and upper values, which are assumed to be the range of uncertainty in the wind tunnel measurements.

In Figures 2.20 and 2.21 one can observe the drag and lift coefficients versus the angle-of-attack α. *XFlow* shows good agreement within the range 1 to 28 degrees, predicting accurately both slope and values of the aerodynamic coefficients. The polar curve in Figure 2.22 is hence matching the experimental results, especially in the pre-stall region. The pitching moment coefficients have been calculated for the range 6 to 34 degrees and also lay between the upper and lower limits of the experimental results, as shown in Figure 2.23.

Eventually, some snapshots of the vorticity flow field are presented in Figures 2.24-2.25.

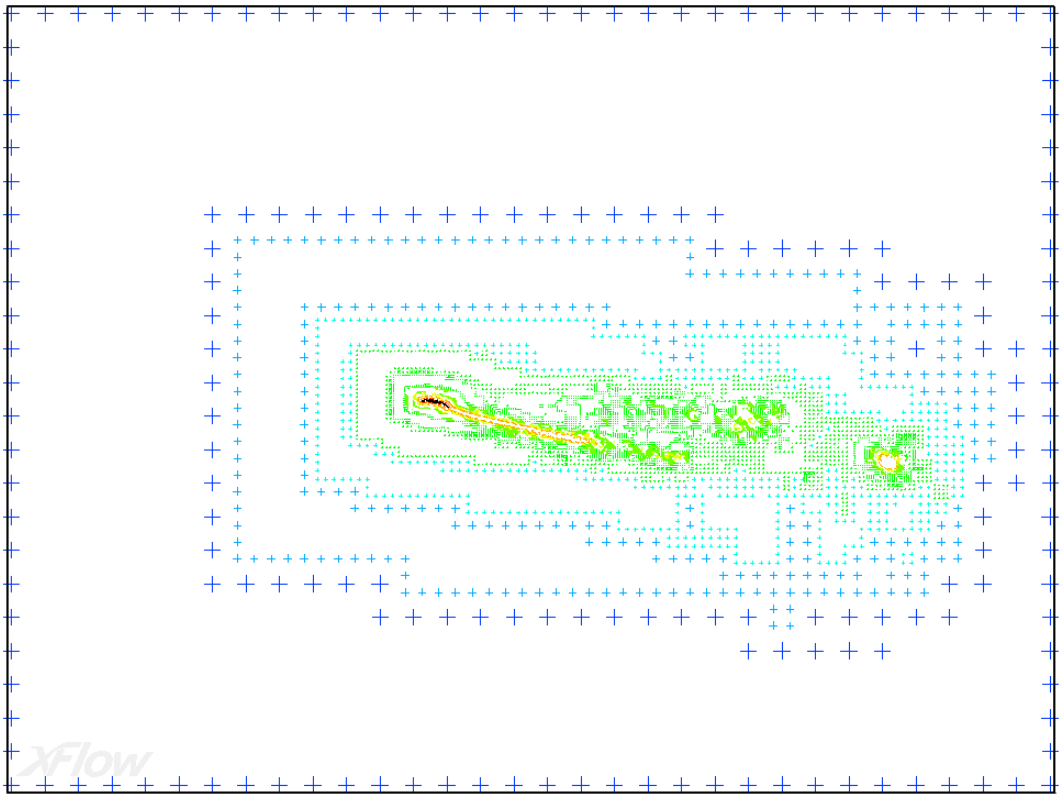

(a)

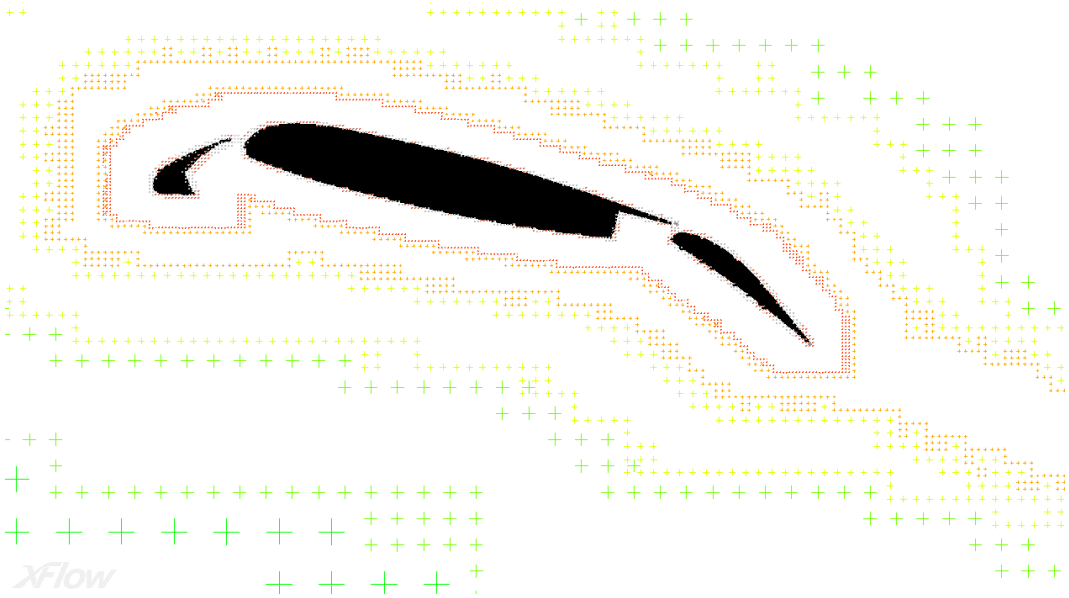

(b)

Figure 2.19: Example of lattice refinement - Resolution 1: (a) virtual wind tunnel and far field resolution, (b) resolution near walls and wake refinement.

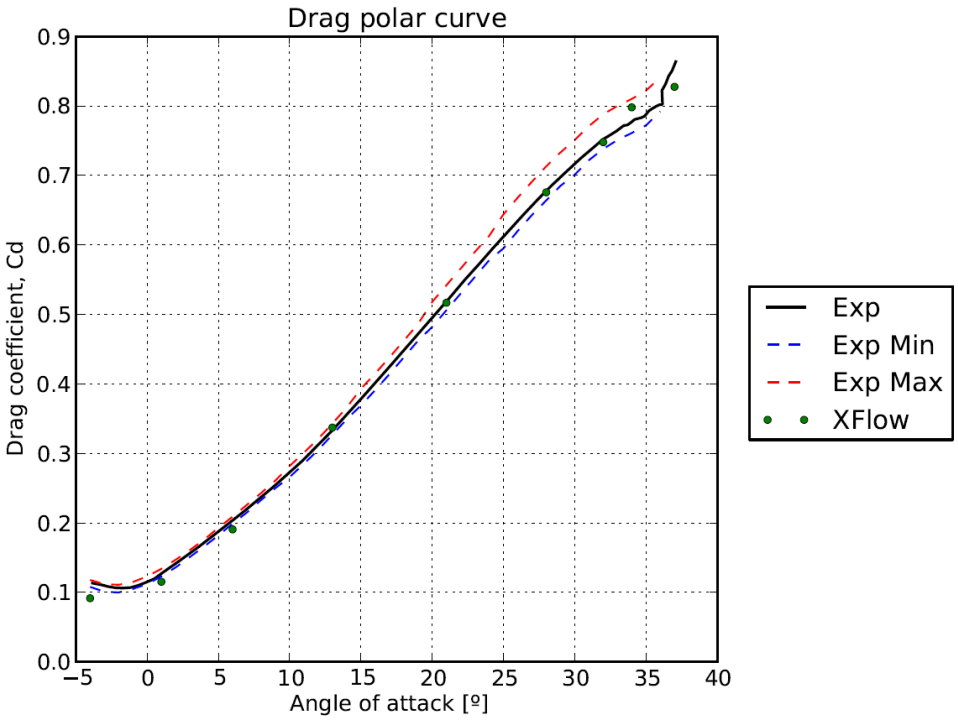

Figure 2.20: Drag coefficient versus angle-of-attack.

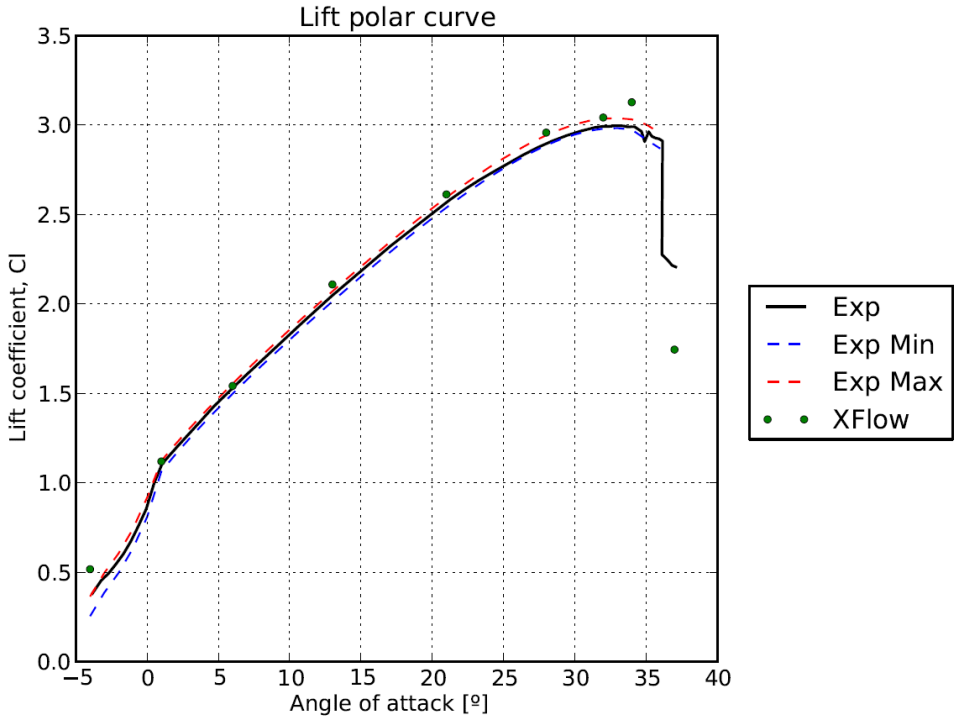

Figure 2.21: Lift coefficient versus angle-of-attack.

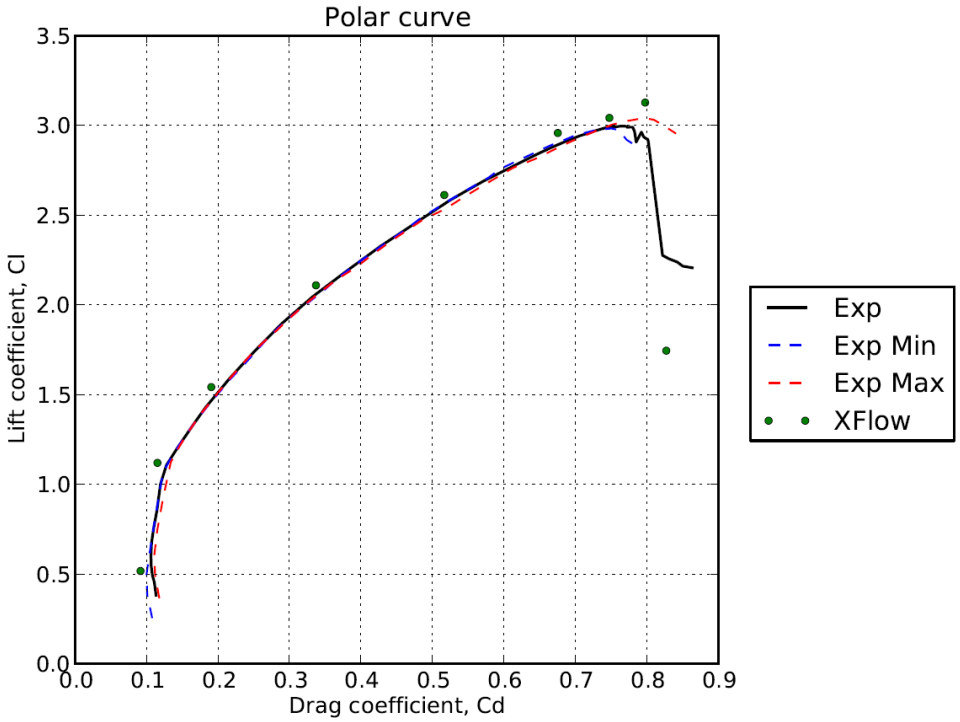

Figure 2.22: Polar curve.

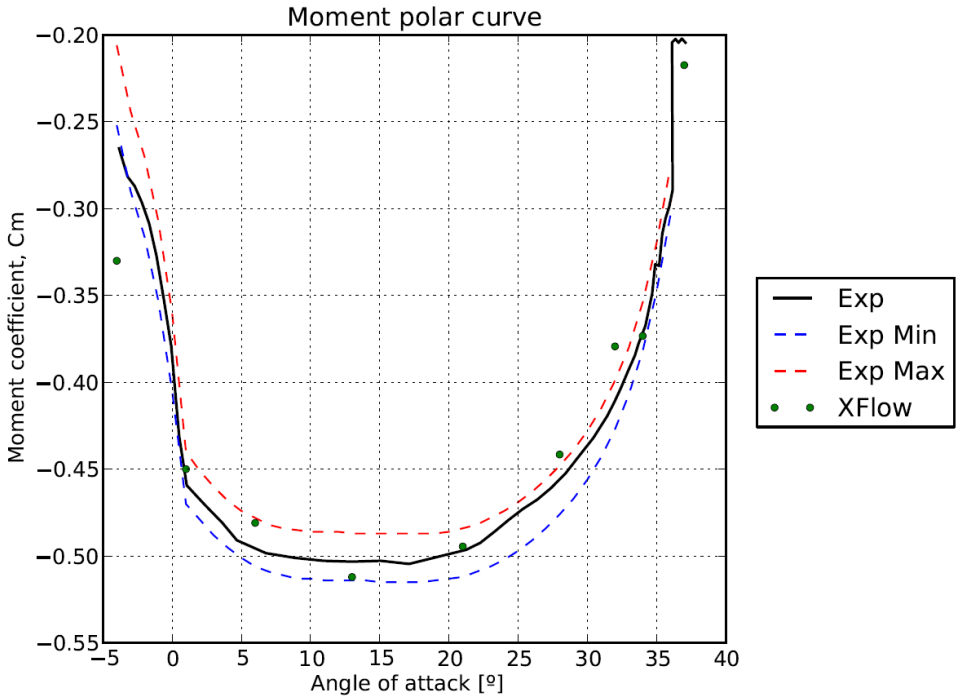

Figure 2.23: Pitching moment coefficient versus angle-of-attack.

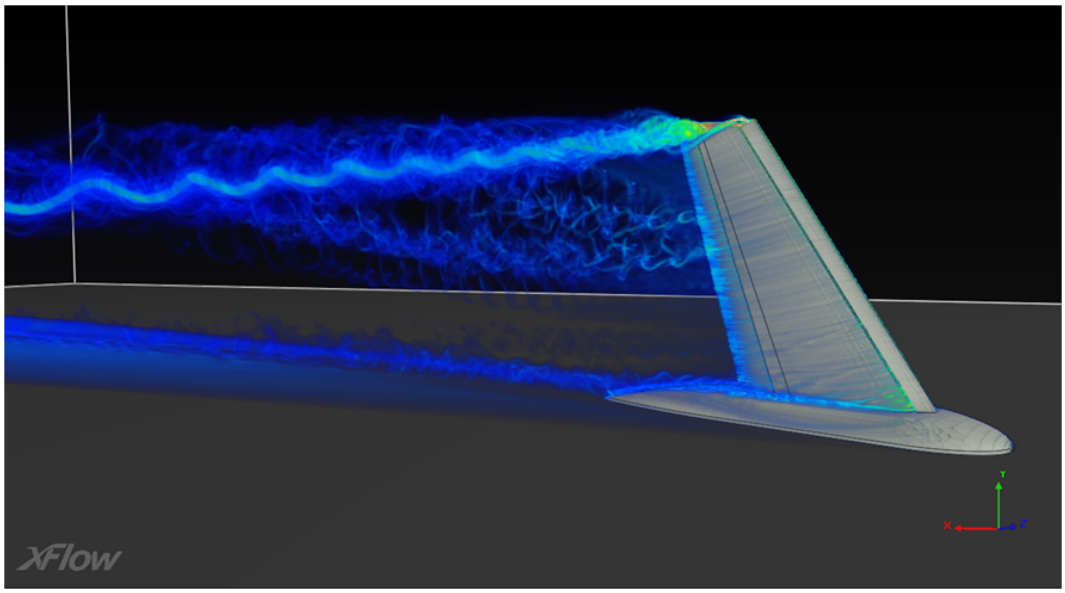

Figure 2.24: Volumetric rendering of vorticity, AoA = 13, upper side.

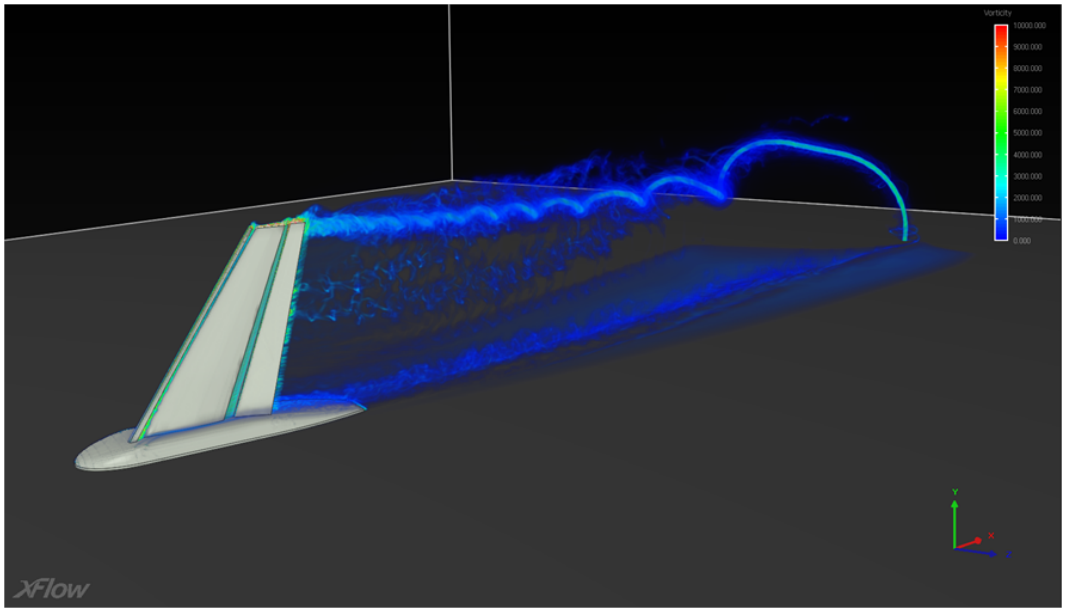

Figure 2.25: Volumetric rendering of vorticity, AoA = 13, lower side.

3 Automotive

Contents

3.1 ASMO

In automotive aerodynamics it is a common practice to use reference geometries to validate CFD codes [13]. This section uses the well known ASMO (*Aerodynamisches Studien Modell*) vehicle model, which comprises a square-back rear, smooth surfaces, boat tailing, underbody diffuser and no pressure induced boundary layer separation. The geometry does not have a well defined separation line and is characterized by a low drag shape.

For this validation the 1/5 wind tunnel test model has been adopted, where vehicle's length, width and height are 0.81 m, 0.29 m and 0.27 m respectively; and wind tunnel dimensions are 18 x 6 x 10 m (see Figure 3.1). This corresponds to a blockage ratio of 0.057%. Experimental data for this test case are available from Daimler Benz and Volvo model scale wind tunnel.

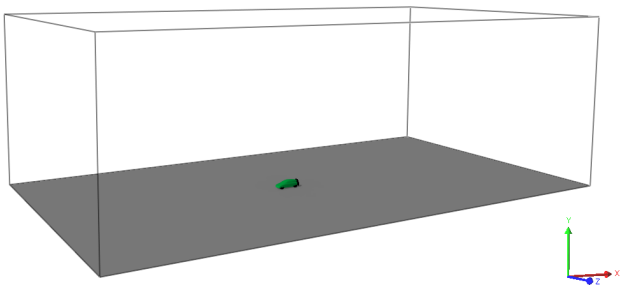

Figure 3.1: ASMO body and wind tunnel geometries.

To perform the simulation, the *XFlow* `Virtual wind tunnel` is used. The inlet-velocity is set to 50 m/s (uniform) and the fluid properties are: density $\rho = 1$ kg m^{-3} and dynamic viscosity $\mu = 1.5 \times 10^{-5}$ Pa s. The Reynolds number is thus 2.7×10^6, taking the length of the vehicle as reference.

In this problem it is essential to properly resolve the turbulent wake. Therefore dynamic wake refinement is applied, so that the specified particle resolution is automatically adopted in regions with high turbulence, while less turbulent regions are treated with fewer particles. Particle resolution in the far field is 0.1 m, whereas scales down to 2.5 mm are resolved in the wake and on the model surface. Turbulence modelling is approached using a Large Eddy Simulation (LES) approach, together with a Wall-Adapting Local Eddy-viscosity (WALE) subgrid model for the turbulent viscosity.

The turbulent wake structure can be observed in Figures 3.2 and 3.3, together with the instantaneous pressure field and the skin friction distribution in Figure 3.4.

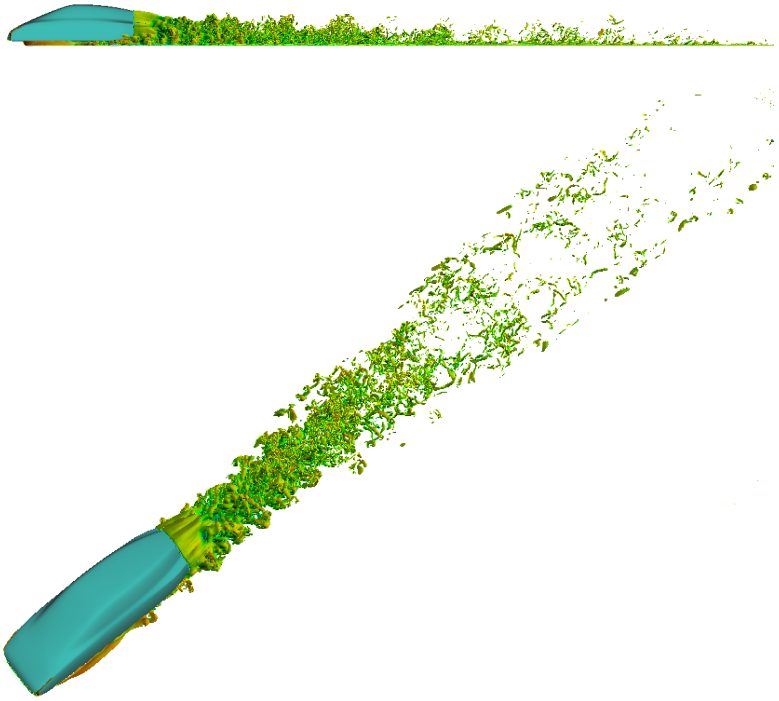

Figure 3.2: Vorticity isosurface.

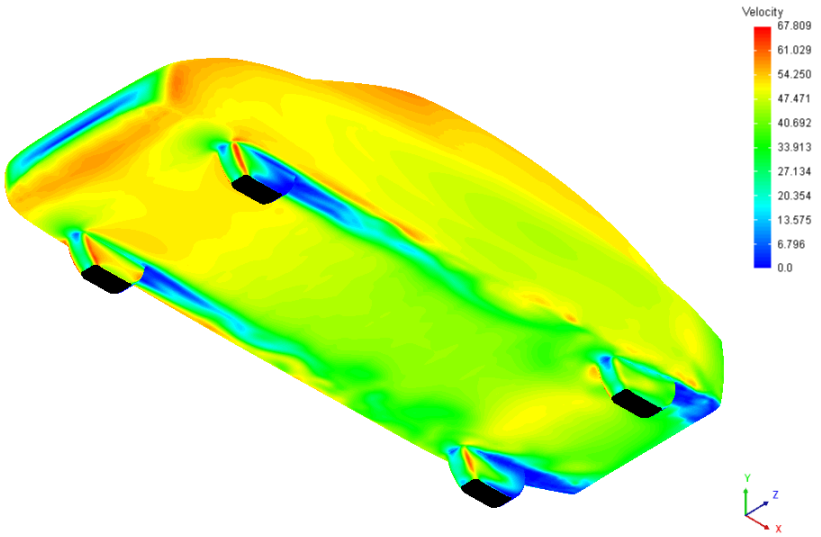

(a)

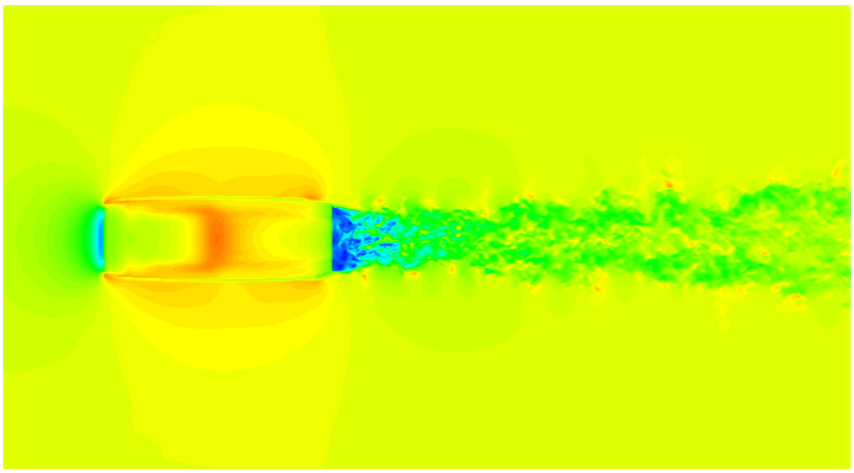

(b)

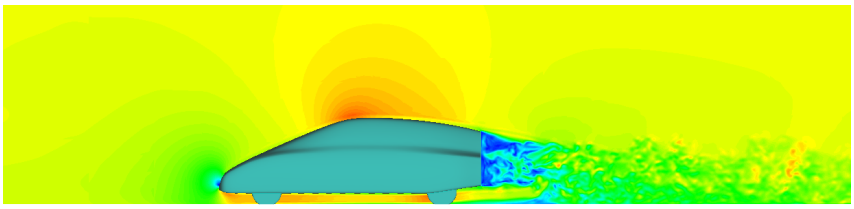

(c)

Figure 3.3: Instantaneous velocity field: (a) on the vehicle surface, (b) in the $Y = 0.07$ m plane, and (c) in the symmetry plane.

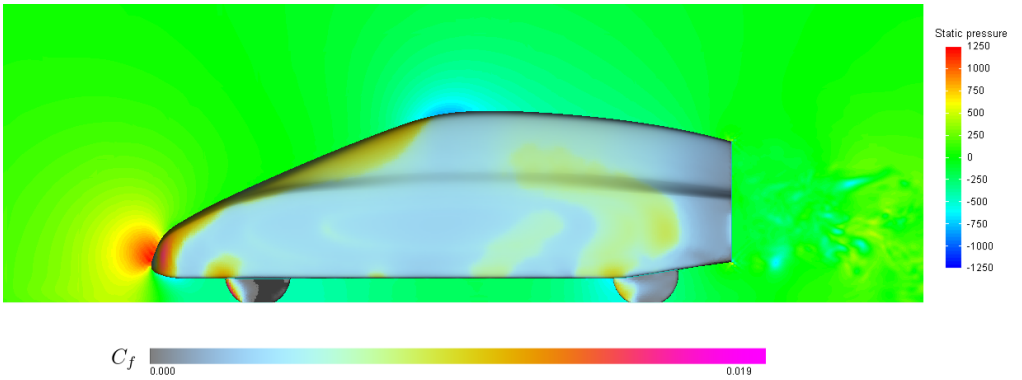

Figure 3.4: Instantaneous pressure field in the symmetry plane and skin friction distribution.

Figures 3.5 to 3.8 show the comparison between the *XFlow* results and the experimental data for the pressure field along the symmetry plane on the front, roof, base and underbody surfaces. It can be seen that the comparison with the measurements is good, although some deviations can be observed especially in the base pressure, which is slightly underpredicted. However the proper level of the base pressure is not known exactly, as there is a large difference between both experiments.

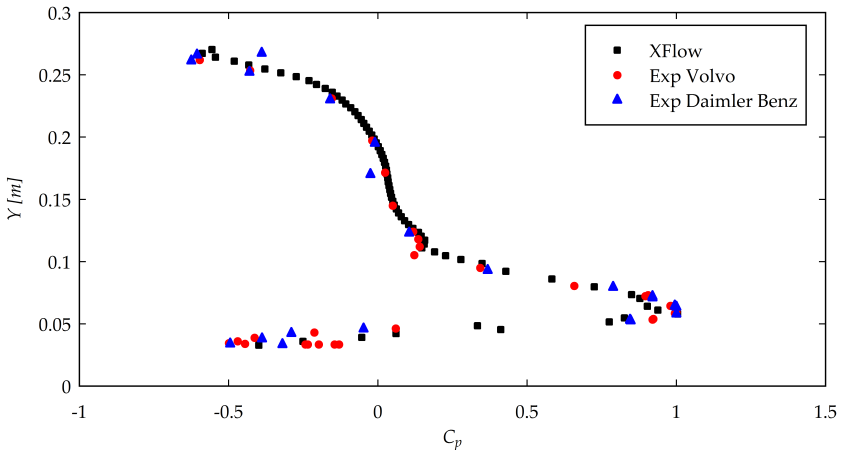

Figure 3.5: Front pressure distribution along the symmetry plane.

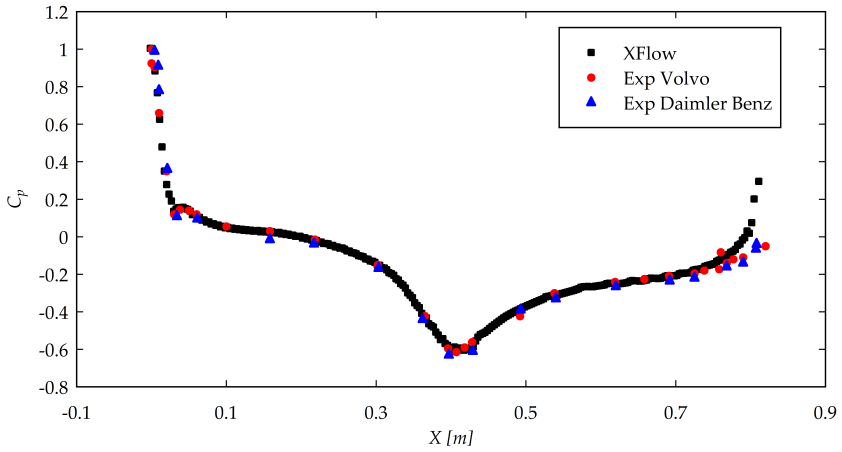

Figure 3.6: Roof pressure distribution along the symmetry plane.

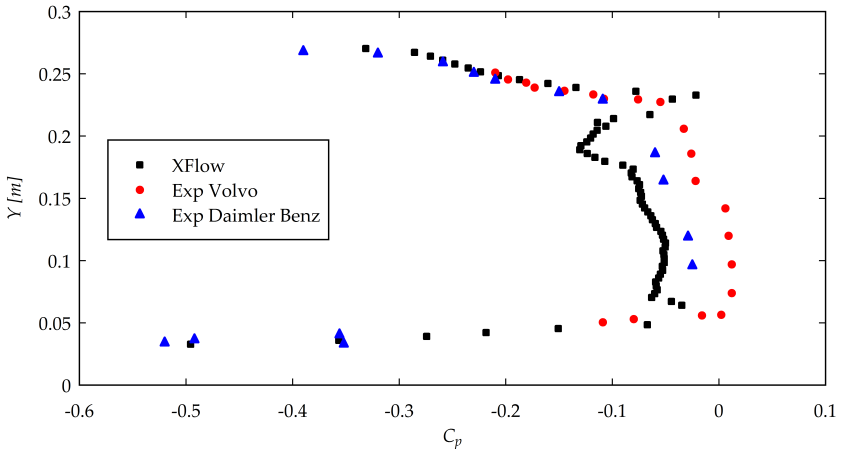

Figure 3.7: Base pressure distribution along the symmetry plane.

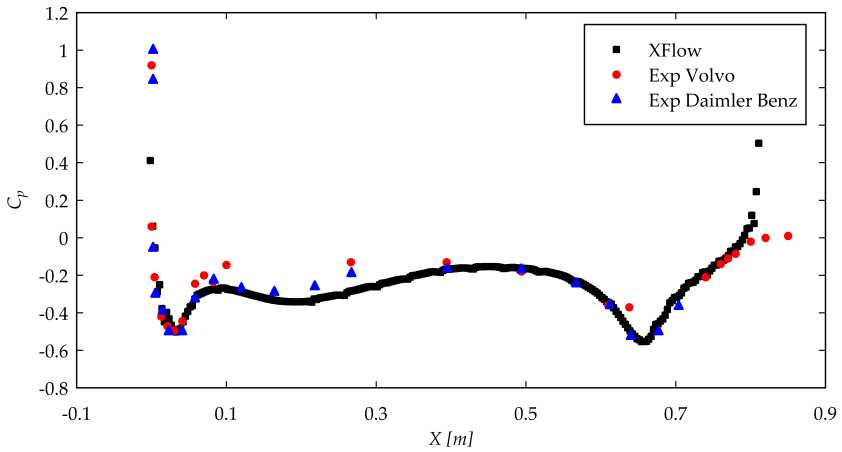

Figure 3.8: Underbody pressure distribution along the symmetry plane.

Typically, drag stabilizes in a characteristic time of the order of the flow travelling the vehicle length. In 0.1 seconds, the flow has travelled more than six times the whole body. The time averaged drag between 0.05 and 0.1 seconds of physical simulation is $C_d = 0.166$ (see Figure 3.9), in good agreement with the values measured in the experiments shown in Table 3.1.

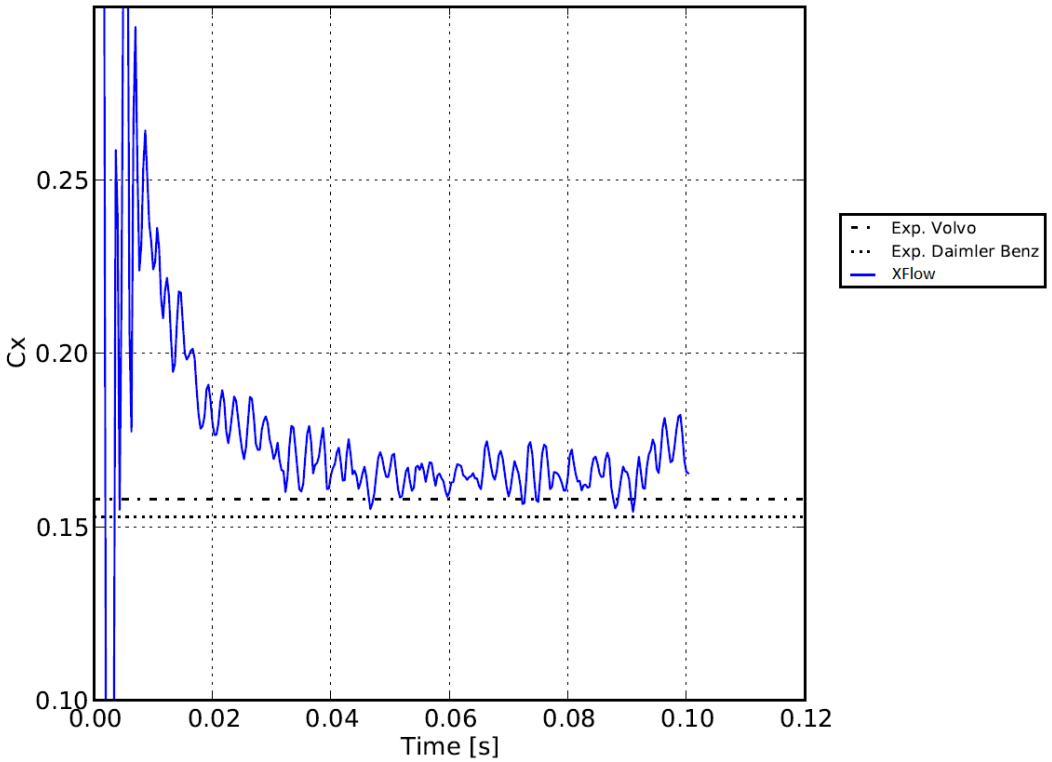

Figure 3.9: Overall drag history.

XFlow	0.166
Experiments Volvo	0.158
Experiments Daimler Benz	0.153

Table 3.1: Drag values for ASMO model.

3.2 Ahmed body for Re=4.29E+6

The Ahmed body is the most classical benchmark in the automotive industry. It has been first defined and its characteristics described in the experimental work of Ahmed [14]. The Ahmed body geometry is described in Figure 3.10. The experimental measurements at various slant angles (φ =[0°,40°]) were conducted by Ahmed and Ramm in the DFVLR subsonic wind tunnels at Braunschweig and Göttingen; these having a square nozzle of (3 x 3) m and a length of 5.8 m.

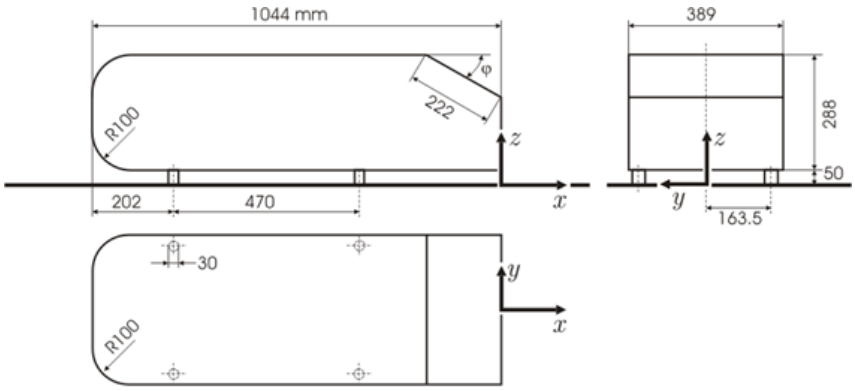

Figure 3.10: Ahmed body geometry, from [15].

The goal of this validation test case is twofold: (i) the validation of the drag curve against the slant angle; and (ii) the analysis of the mean turbulence structures on the slant surface of the Ahmed body and in the downstream region. To this end, the geometry shown in Figure 3.10 has been simulated with *XFlow* using the 3D single-phase engine and a virtual wind tunnel of dimensions 8 x 2 x 2 m as a external domain. The wall ground was activated with zero velocity.

In order to reach a Reynolds number based on the car length equal to 4.29 million, the simulation parameters have been set according to Table 3.2.

Firstly, the mesh dependency of the drag coefficient is studied to find a trade-off between accuracy and computing time. In this study the far field resolution is set to 0.08 m, whereas the walls and wake resolution level is varied according to the values given in Table 3.3.

Figure 3.11 shows the variation of the drag coefficient (C_x) calculated by *XFlow* for the different refinement levels together with the experimental value. It turns out that the wall resolution level h/2^2 (0.01 m) gives good results and in an acceptable time. Figure 3.12 shows the value of the drag coefficient (C_x) calculated by *XFlow* for the different wake refinement levels, keeping the wall-resolution to 0.01m. From the figure, the best resolution for the wake is also 0.01 m. Henceforth, the spatial discretization for all cases is set to *Adaptive refinement* with a resolution of 0.08 m

Project tree parameter	Value
Inlet velocity [V_{ref}]	60 m s^{-1}
Density [ρ]	1 kg m^{-3}
Dynamic viscosity [μ]	1.46014e-5 Pa s
Car length [L_{ref}]	1044 m
Reynolds number [Re]	4.29e+6
Slant Angles [φ]	0°; 5°; 10°; 12.5°; 15°; 20°; 25°; 30°; 32°; 35°; 40°
Turbulence Intensity	0.5 %
Simulation time	2.0 s
Courant number	1 s

Table 3.2: Simulation settings

$\varphi = 35°$	h	h/2	$h/2^2$	$h/2^4$
Resolution [m]	0.04	0.02	0.01	0.005
Initial number of elements	72853	103267	219457	676854

Table 3.3: The initial number of elements for the different resolutions, case $\varphi = 35°$

in the far field and 0.01 m around the Ahmed body and wake.

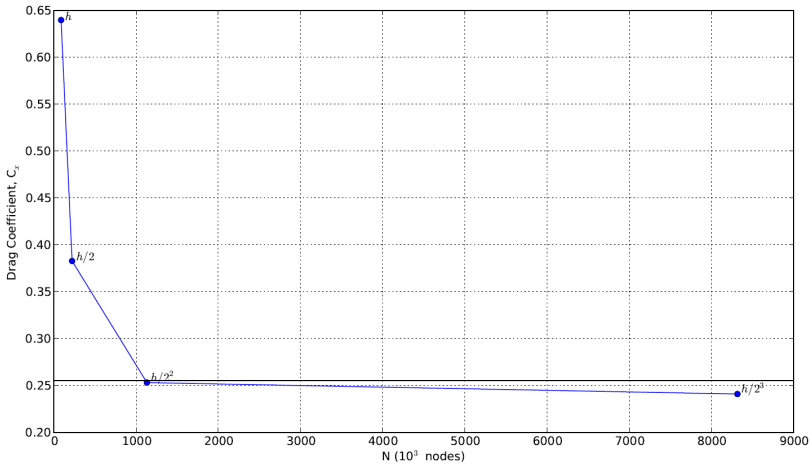

Figure 3.11: Near-wall resolution dependency of the drag coefficient for φ= 35°

The first part of validation is about comparing the Ahmed-body drag-coefficient value obtained with *XFlow* with that measured by Ahmed and Ramm [14]. Figure 3.13 shows the drag coefficient obtained with *XFlow* superposed on the experimental drag curve by Ahmed and Ramm [14]. *XFlow* and experimental drag curves agree with a good accuracy and the minimum drag angle found is for 12.5 degrees slant angle as expected. An additional point around 29 degrees would be required to

confirm the drag peak around 30 degrees.

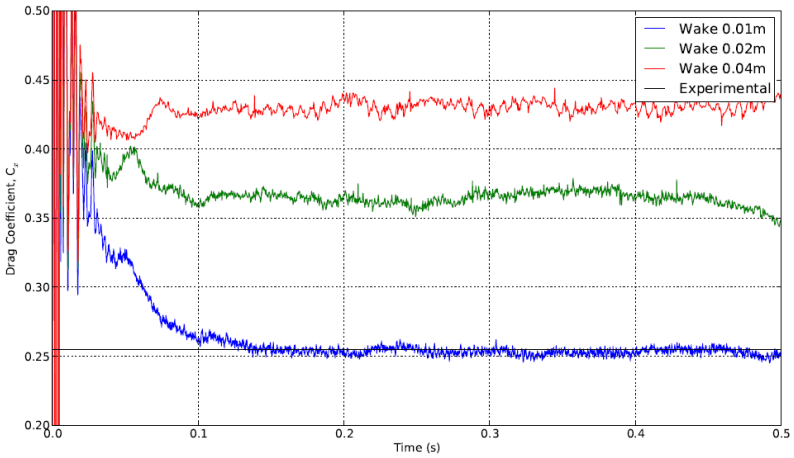

Figure 3.12: The influence of the wake resolution on the drag coefficient for $\varphi = 35°$

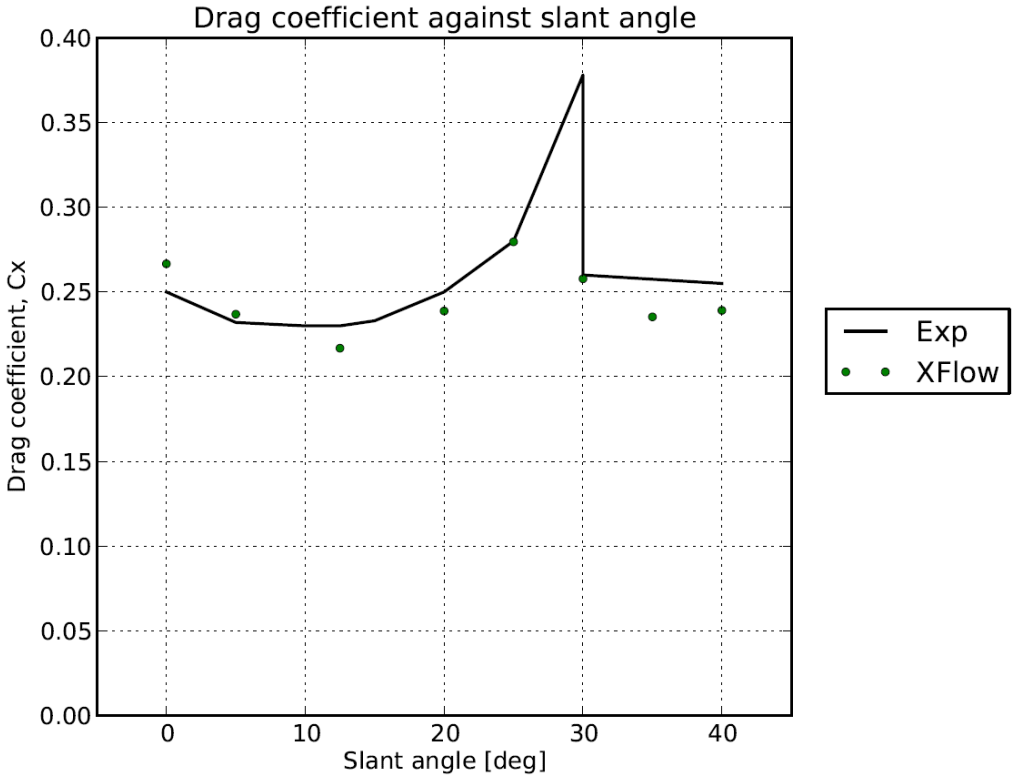

Figure 3.13: Drag coefficient against slant angle

The second part of validation is about analysing the main turbulence structures around the Ahmed Body. According to Franck et al. [16], the experiments show two critical slant angles: $\varphi = 12.5°$ and $\varphi = 30°$, called first and second critical angles respectively; where the main structure of the time-averaged flow in the near-wake

changes significantly. Between these two critical angles, the flow is massively 3D separated, for other slant angles the flow is almost 2D attached to the body. This behaviour is perfectly reproduced by *XFlow* as shown in Figure 3.14.

Ahmed and Ramm [14] also provides some pictures of the flow streamlines on the slanted surface. Figure 3.2 shows both Ahmed and *XFlow* streamlines for the same slant angles. It can be seen that the *XFlow* streamlines present the same main structures than those captured experimentally [14].

The validation of the Ahmed body case with *XFlow* confirms its good performance for aerodynamic applications with high Reynolds numbers. The time required in *XFlow* to set up a case is about 5 minutes. The calculation takes about 6-8 hours on a machine equipped with 16 CPUs. This time is almost constant for all the slant angles.

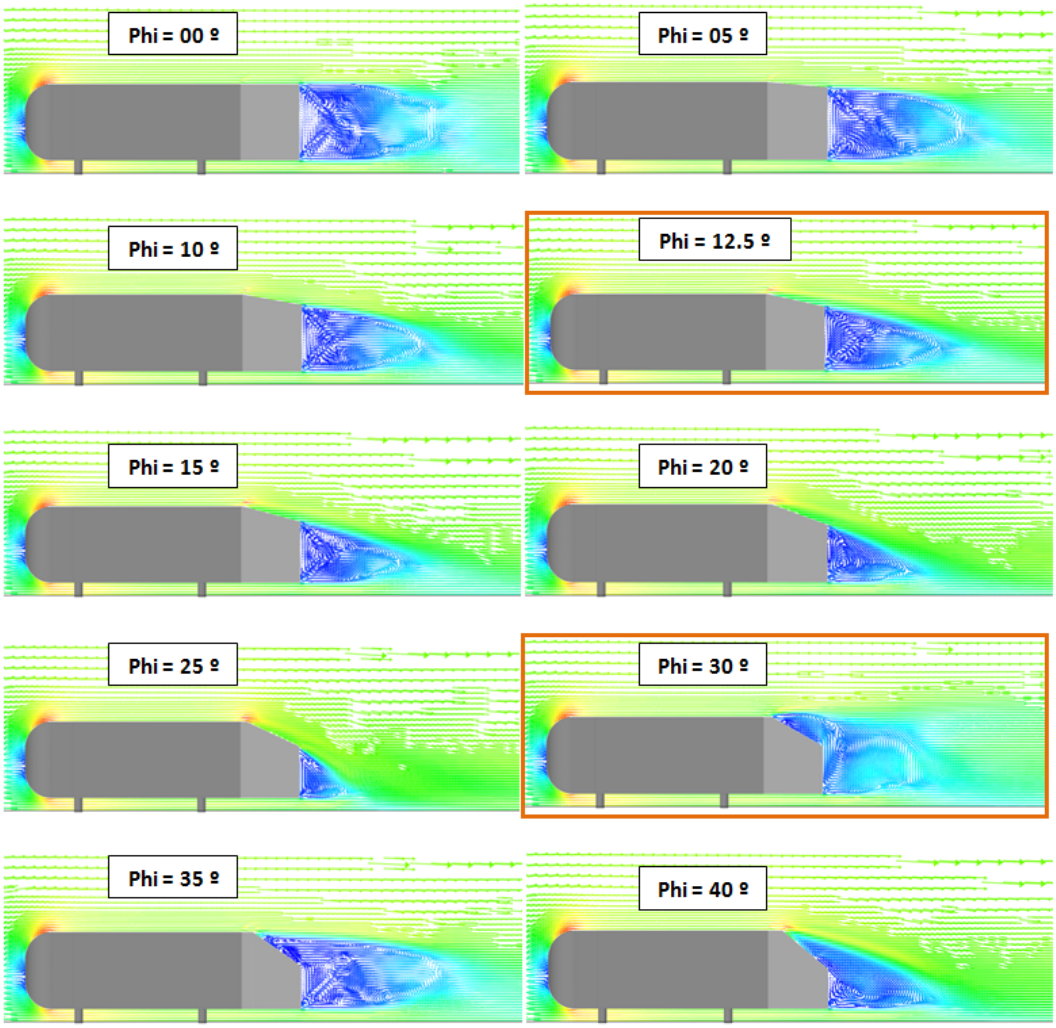

Figure 3.14: Time-averaged flow for the different slant angles (critical angles are outlined in red).

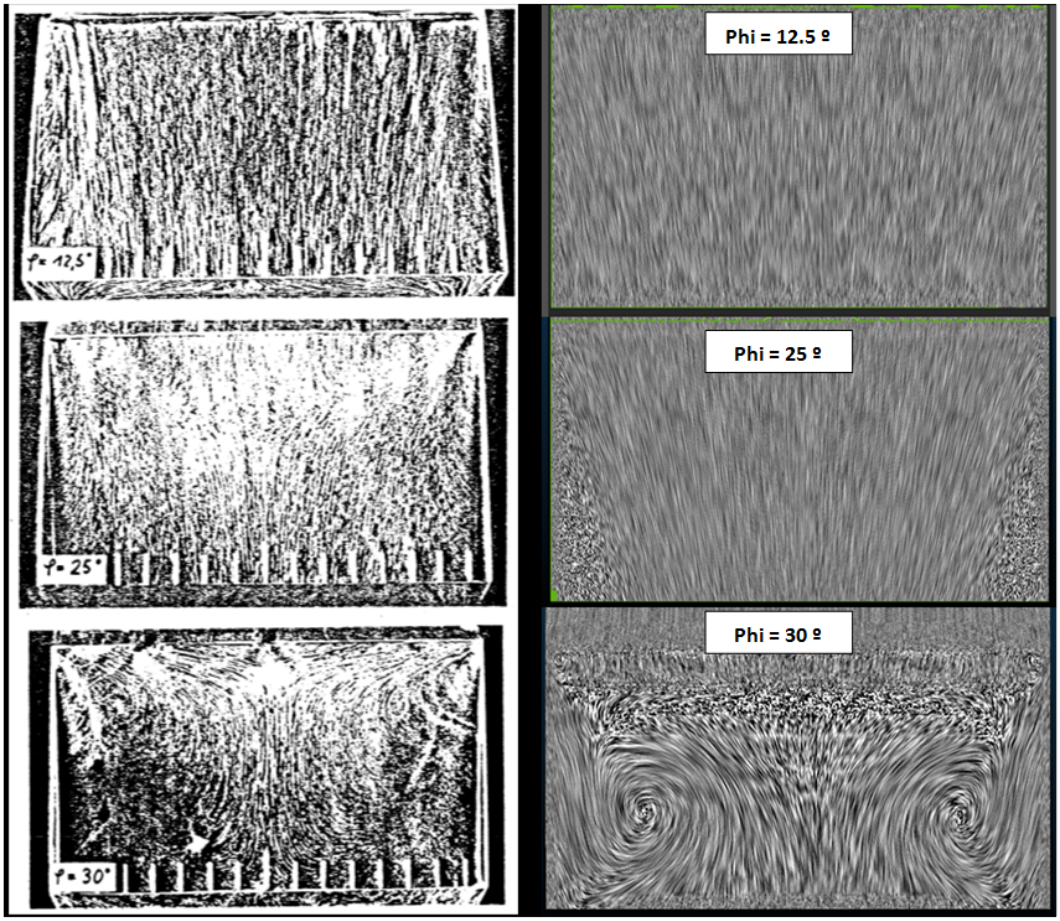

Figure 3.15: Streamlines on the rear surface for $\varphi = 12.5°$, $25°$ and $30°$, from [14].

4

Free surface

Contents

4.1 NACA-0024 hydrofoil

In order to validate the *XFlow* free-surface engine, it is used to simulate the test-case of a surface-piercing NACA-0024 hydrofoil. Numerical results are compared with the experimental data reported by Metcalf et al. in [17].

The experiments were conducted in a towing tank for three different flow regimes, namely: $Fr = 0.19, 0.37, 0.55$; Fr being the Froude number based on the NACA chord length (L):

$$Fr = \frac{V_{ref}}{\sqrt{gL}} \tag{4.1}$$

V_{ref} represents the NACA velocity and g the gravity. To facilitate the flow field measurements, the NACA-0024 foil chord ($L = 1.2$m) and draft ($T = 1.5$m) were designed to achieve a large separation region and no-wave effects and 2D flow at large depths [17]. Some photographs of the experiments are shown in Figure 4.1.

The *XFlow* 3-D Free-Surface external solver has been used to reproduce numerically the experimental test case corresponding with a Froude number of 0.37. To reach such a Froude number, the simulation parameters have been set according to Table 4.1; temporal and spatial discretisation details are also given in Table 4.1.

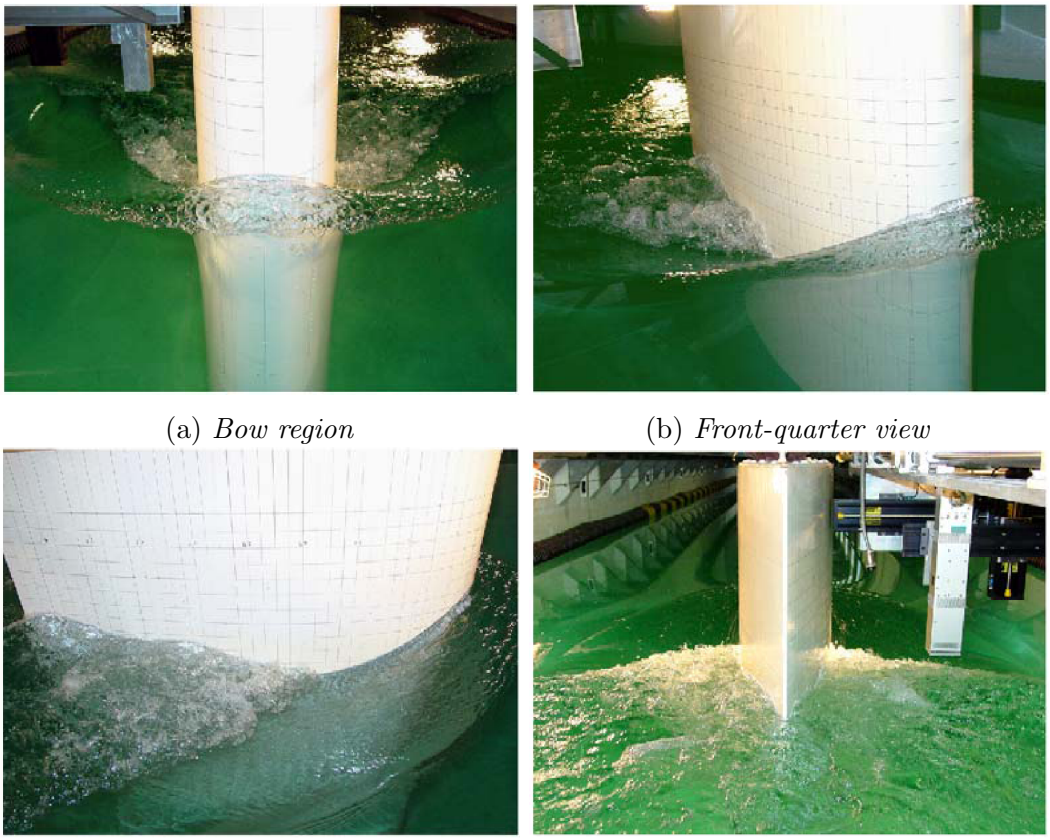

(a) *Bow region* (b) *Front-quarter view*

(c) *Side view of wave profile* (d) *Wake region*

Figure 4.1: Photographs of the NACA 0024 wave field for $Fr = 0.37$, from [17].

Project tree parameter	Value
Gravity $[g]$	9.81 m s^{-2}
Inlet velocity $[V_{ref}]$	(1.27, 0, 0) m s^{-1}
Density $[\rho]$	998.3 kg m^{-3}
Dynamic viscosity $[\mu]$	0.001 Pa s
NACA-0024 chord length $[L_{ref}]$	1.2 m
NACA-0024 behaviour	Fixed
Simulation time	20.0 s
Courant number	1 s
Resolved scale	0.2 m
Refinement algorithm	Adaptive refinement
Wake refinement threshold	Automatic
Wake resolution	0.0125 m
Shape refinement	0.0125 m

Table 4.1: Relevant simulation settings

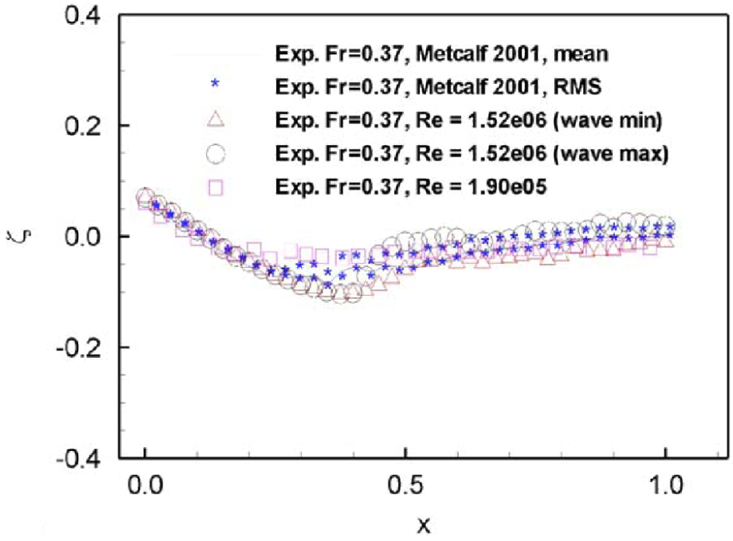

(a) *Experimental data*

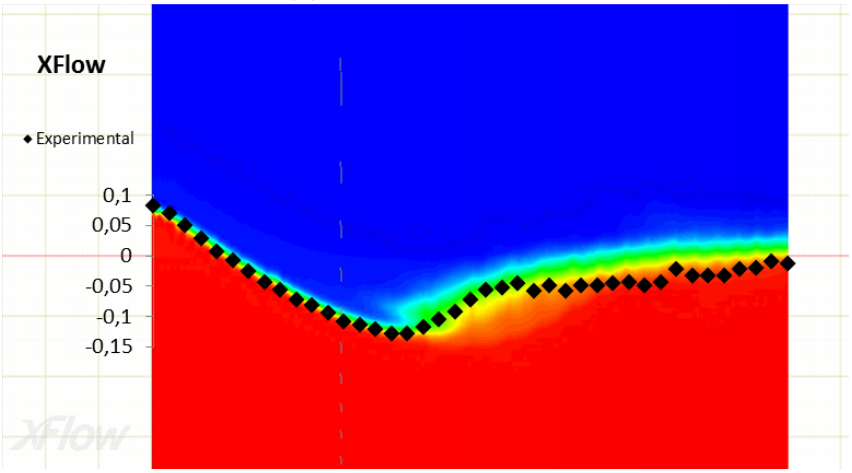

(b) *Experimental and numerical averaged contour overlapped*

Figure 4.2: Wave profiles and near-field elevations close to the foil surface for $Fr = 0.37$.

Figure 4.2(a) shows the contours of the z-coordinate on the free surface, illustrating the varying height of the free surface along the hydrofoil. In Figure 4.2(b) the computed free surface (averaged over the period [0s; 19.7s]) is compared with experimental data, finding a good match.

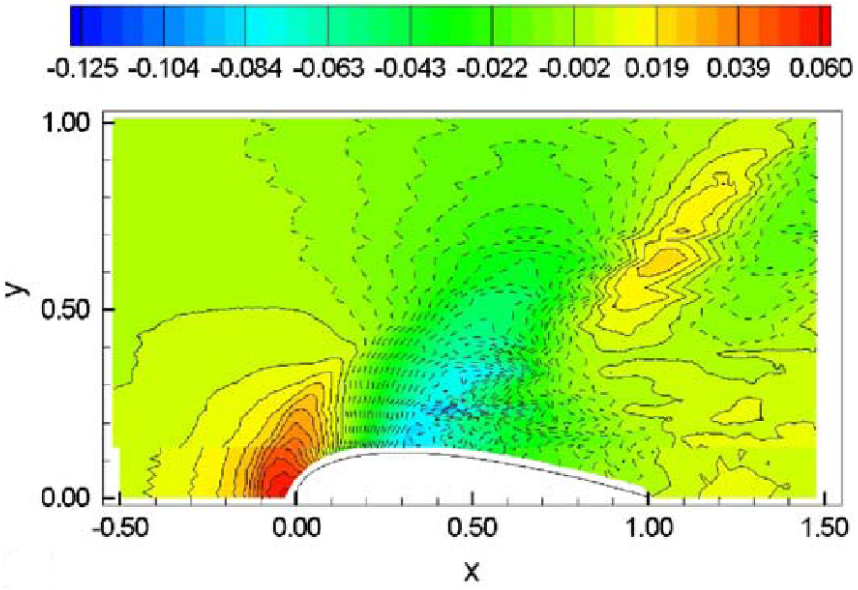

(a) *Experimental data*

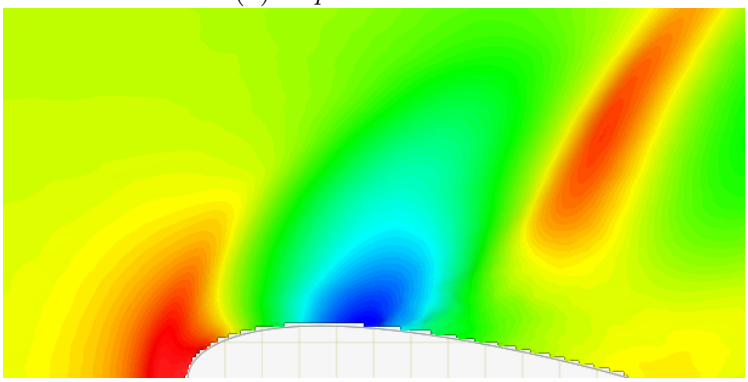

(b) *Numerical averaged*

Figure 4.3: Free-surface elevation - mean for $Fr = 0.37$.

Figures 4.3(a) and Figure 4.3(b) show the experimental and numerical mean free-surface elevation contours on the x-y plane. Qualitative agreement is found.

4.2 Dam-Break 3D

The dambreak is a popular validation case for free surface flows, since no special in-/out-flow boundary conditions are needed. In this section, *XFlow* free-surface-internal engine is validated by comparing the *XFlow* results with the experimental data from the Maritime Research Institute Netherlands (MARIN) [18].

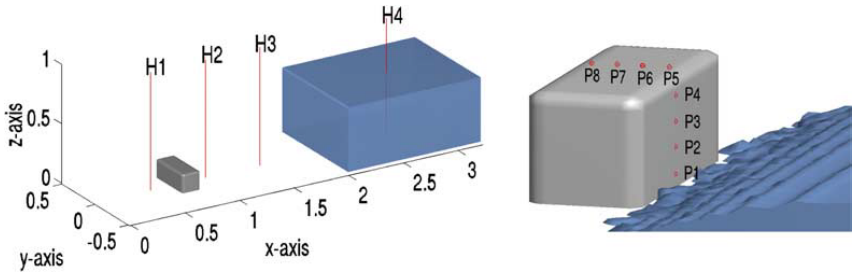

Figure 4.4: Measurement positions for water heights and pressures in the dambreak experiment

The experiment is performed using a large tank (3.22 x 1 x 1 m) with an open roof. The right part of the tank is first closed by a door. Behind the door 0.55 m of water is waiting to flow into the tank when the door is opened. This is done by releasing a weight, which almost instantaneously pulls the door up. In the tank a box has been placed that represents a scale model of a container on the deck of a ship. During the experiment measurements have been performed of water heights, pressures and forces. In Figure 4.4 the positions of the measured quantities are shown. Four vertical height probes have been used; one in the reservoir and the other three in the tank. The box was covered by eight pressure sensors, four on the front of the box and four on the top [18]. Two images of the experiment are shown in Figure 4.5.

Figure 4.5: Pictures taken during the experiment, at time 0.4 (left) and 0.56 s (right)[18].

Table 4.2 shows the relevant parameters used to run the *XFlow* simulation, whereas

Project tree parameter	Value
Engine	3D Free Surface Internal (Isothermal)
Gravitational potential	Off
External acceleration laws	9.81 m s^{-2}
Initial liquid function	if ($x < 0$, 0, $y < 0.55$)
Initial velocity field	(0 0 0) m s^{-1}
Initial gauge pressure	0 Pa
Density [ρ]	1000 kg m^{-3}
Dynamic viscosity [μ]	0.001 Pa s
Tank behaviour	Fixed (Wall boundaries)
Simulation time	7.2 s
Courant number	1
Resolved scale	0.01 m
Refinement algorithm	Disabled

Table 4.2: Relevant simulation settings

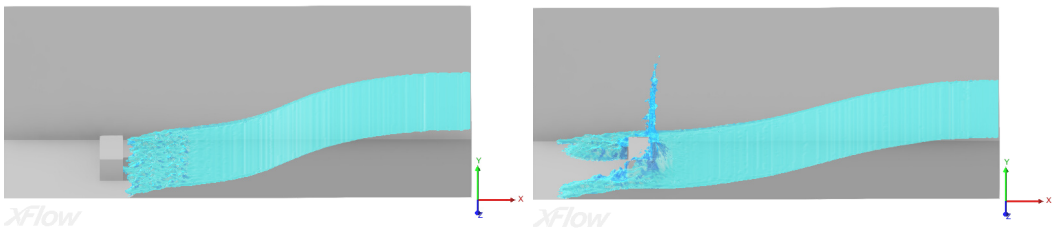

Figure 4.6: *XFlow* free-surface at time 0.4 s (left) and 0.56 s (right).

Figure 4.6 shows the numerical free surface corresponding to the same instants of time at which the pictures in Figure 4.5 were taken. Comparing these two figures, it can be observed that there is a good qualitative agreement between numerical and experimental free-surface shapes. For a quantitative validation, the experimental pressure on the box surface measured by eight sensors (four on the front and four on the top) is next compared with the *XFlow* results.

Figures 4.7 and 4.8 show the quantitative comparison of the experimental and numerical pressure at the sensors positions. Figure 4.7 shows a very good agreement between numerical and experimental data agree at the box front measurement points. As shown in Figure 4.8, this agreement is also found at the sensor positions on the top of the box, though it is less accurate.

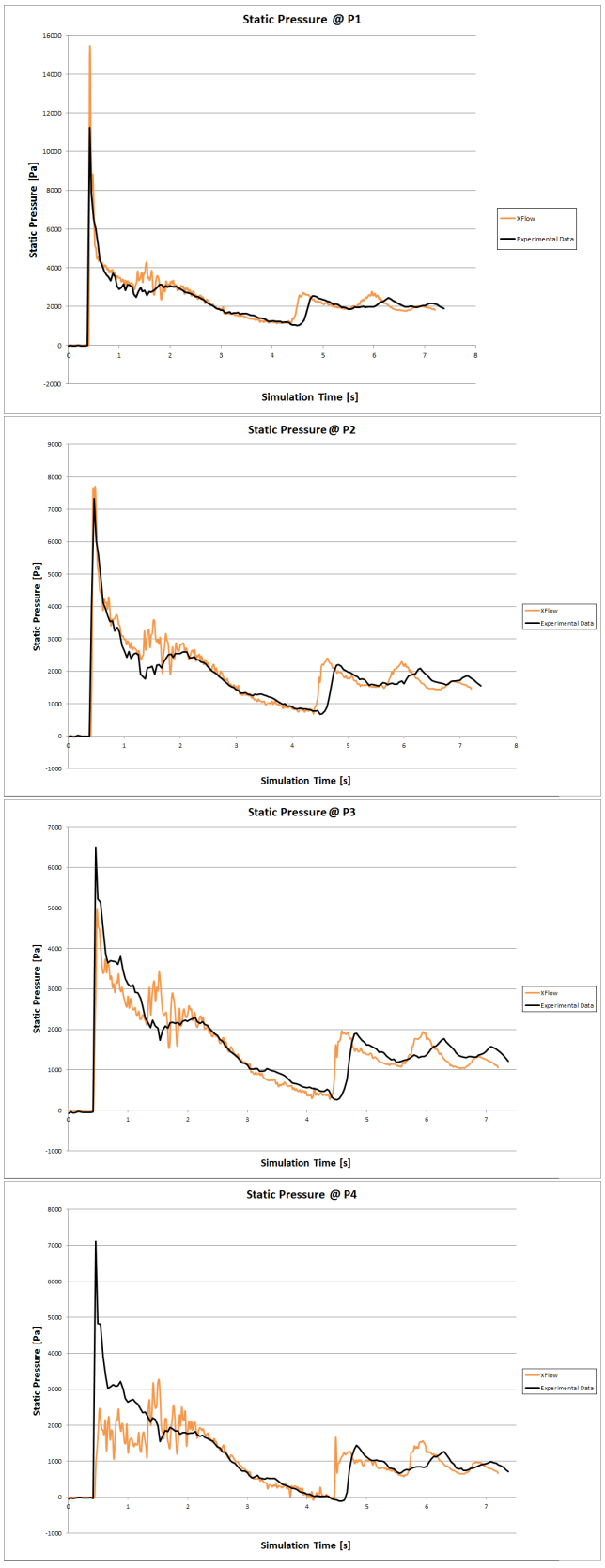

Figure 4.7: Static Pressure at four points of the box front (P1, P2, P3, P4)

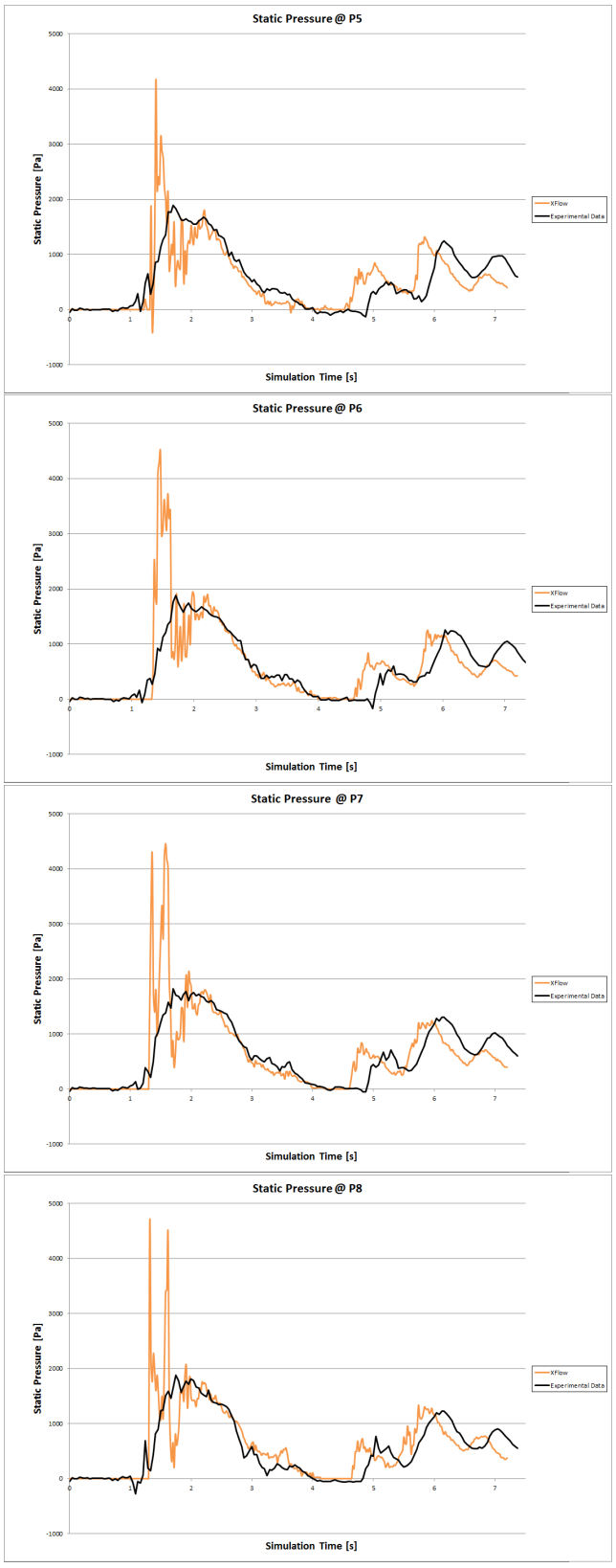

Figure 4.8: Static Pressure at four points of the box top (P5, P6, P7, P8)

4.3 SYSSER50 hydrodynamics

The Delft Systematic Yacht Hull Series (DSYHS) has been started in 1973 by professor J. Gerritsma, in cooperation with N. Newman and J. Kerwin of the Massachusetts Institute of Technology (MIT). The aim is to perform measurements on a series of systematically varied yacht hulls, in order to assess the influence of the varied parameter on the hydrodynamic performance (resistance, seakeeping etc.) of a sailing yacht hull. The model SYSSER50 is part of this series and its experimental data is available on DSYHS Database website.

The boat length is 2.375 m, the width is 0.737 m, and the thickness is 0.336 m. The boat is located into the *XFlow* water channel of dimensions (15, 2, 4) m. The illustration of the problem setup is depicted Figure 4.9. The aim of the study is to recover the hull resistance force and compare it with the experimental data from DSYHS. Besides, it has been took the opportunity to check the wave pattern angle that is left behind by a ship at sea. This angle was first determined by Lord Kelvin [19], where the value is $\theta = 19.28°$.

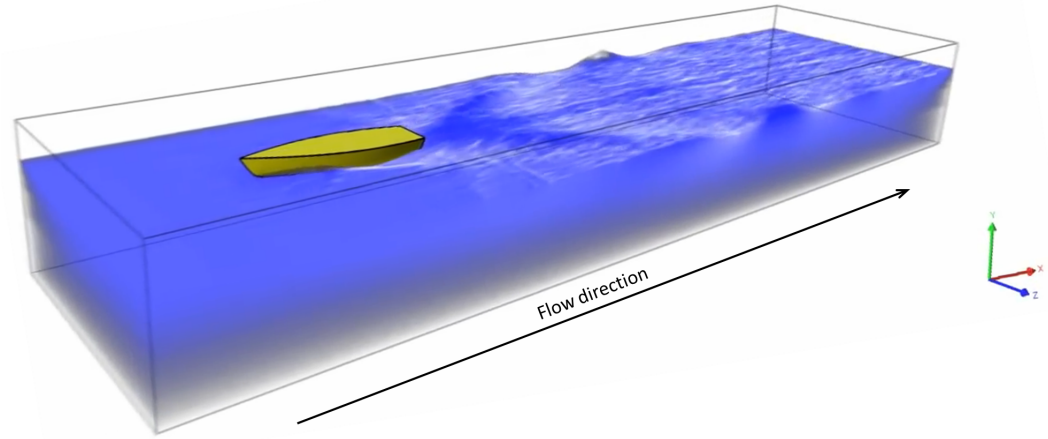

Figure 4.9: Water flow around the SYSSER50 geometry in the *XFlow* water channel.

The flow model used is free surface external, and the fluid gravity is set to -9.81 m/s in Y direction. The inlet is set as constant velocity and height, providing flat sea conditions. The case is run for several velocities, as indicated Table 4.3. The hull geometry behavior in *XFlow* is set to *Rigid body dynamics* with one degree of freedom on the heave motion. The pitch angle is fixed and set to the value found in the DSYHS data. Initial heave position is set to 0 m in Y direction, and will stabilize after the transient period according to the gravity applied on the geometry weight and the inlet water velocity.

The simulation time is set to 7 seconds, with automatic time step. The refinement algorithm is set to *Adaptive refinement* in order to refine dynamically the wake, the

Free-stream velocities	v_{ref}	1.109 m s^{-1}
		1.700 m s^{-1}
		1.990 m s^{-1}
		2.439 m s^{-1}
		2.880 m s^{-1}
		3.099 m s^{-1}
Density	ρ	998 kg m^{-3}
Dynamic viscosity	μ	0.001 Pa s
Reference area	A_{ref}	0.917 m^2
Geometry behavior		Rigid body dynamics
Geometry density		156 kg m^{-3}
Geometry mass		47.5 kg

Table 4.3: Simulation conditions.

moving hull, and the free surface. The resolutions are detailed in Table 4.4, and the resulting lattice structure is shown Figure 4.10.

Refinement Algorithm	Walls	Wake/Free Surface	Far Field
Adaptive refinement	0.015625 m	0.015625 m	0.5 m

Table 4.4: Spatial discretization.

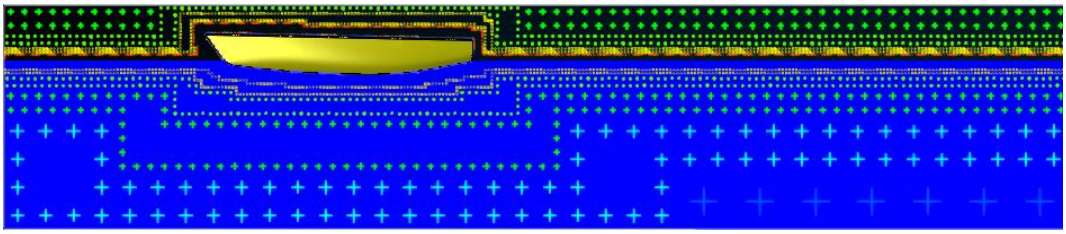

Figure 4.10: Initial lattice structure.

The simulations run on 12 cores in about 30h for every velocity point. The force histories are converging after 3 seconds of simulation time for low water speeds, and after 6 seconds for medium and high water speeds. The convergence can be appreciated Figure 4.11 and is quite stable. This transient period is the time required for the boat to stabilize the heave, and obviously takes longer when the water speed is higher.

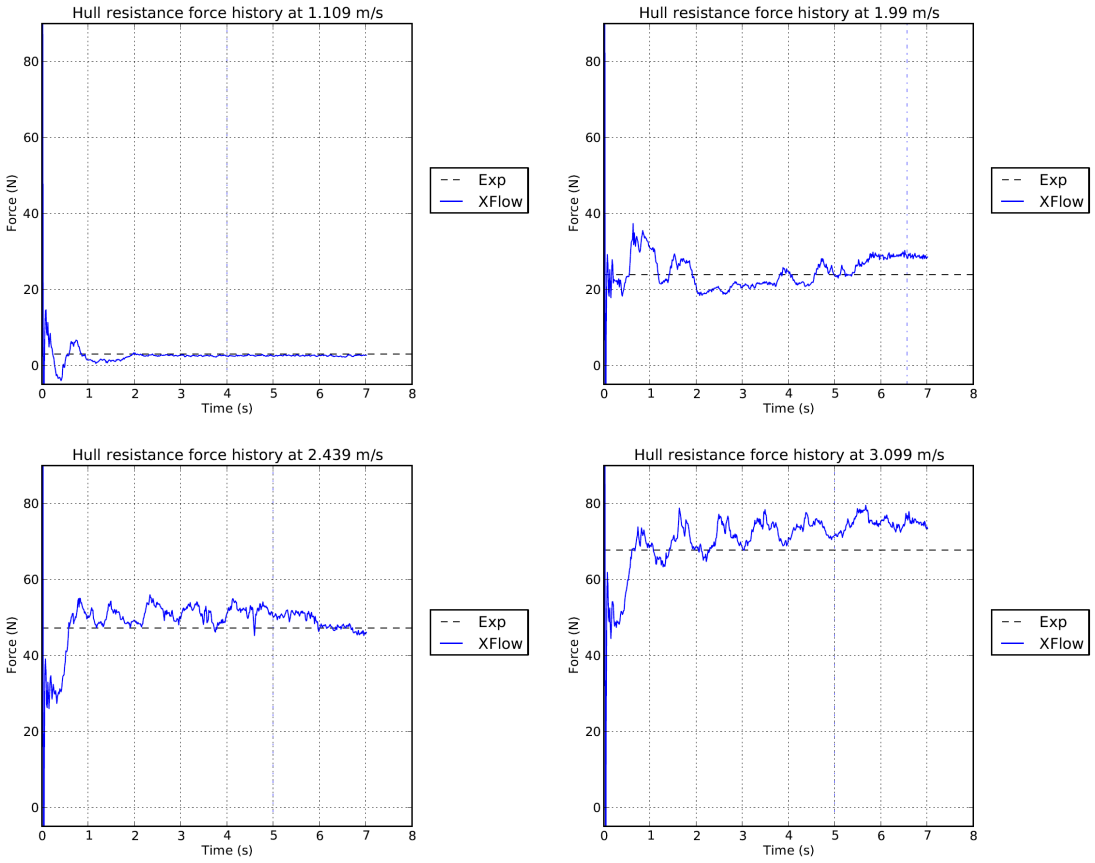

Figure 4.11: Hull resistance force histories for 1.109, 1.99, 2.439, and 3.099 m/s.

Since *XFlow* is unsteady, the hull resistance force must be time-averaged. The forces are averaged for every velocity point, starting from the end of the transient period until the end of the simulation. The comparison of the force in Newton and the force coefficient C_x against the velocity is shown on Figure 4.12, and compared with experimental results. The correlation with experimental data is good, the resistance force curve trend is similar since the linear slope is reproduced by *XFlow*. The low velocity point also shows a lower curve slope as expected, and the higher velocity points also decrease despite of being slightly overestimated.

Finally, the wave pattern angle is compared against the theoretical value determined by Kelvin in the Figure 4.11. For the inlet velocity of 2.439m/s *XFlow* provides an accurate wave pattern angle, $\theta = 19.50°$, where the relative error is 1.14%. The rest of velocities have a similar wave pattern angle.

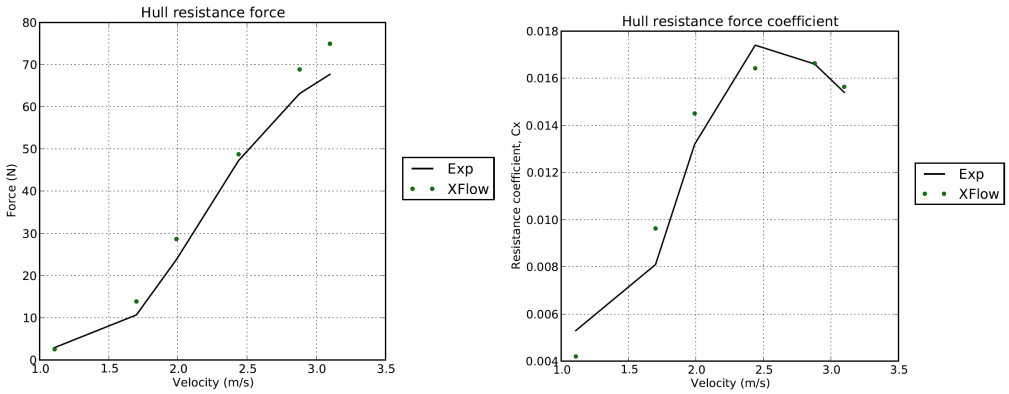

Figure 4.12: Comparison of forces and coefficients against experimental data.

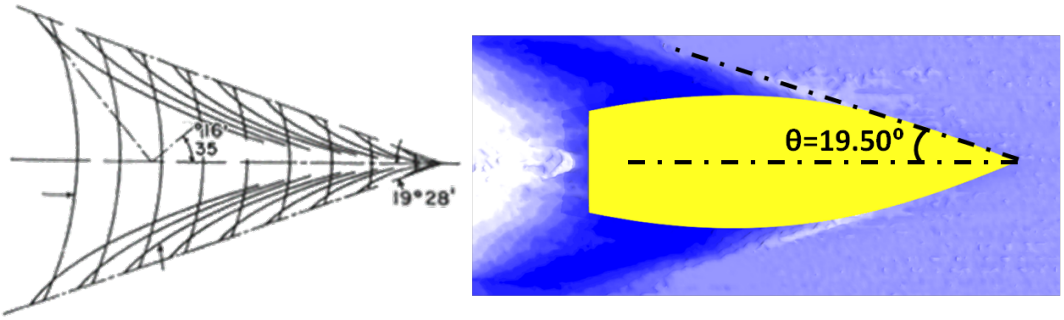

Figure 4.13: Comparison of wave pattern Kevin angle with theoretical value for 2.439 m/s.

5 Acoustics

Contents

5.1 Simple Expansion Chamber

Reactive mufflers operate by the destructive interference of the acoustic waves propagating within them. The simplest type of reactive muffler is the simple expansion chamber, shown in Figure 5.1.

The aim of the present test-case is to validate the *XFlow* acoustics analysis by predicting the transmission loss in a simple expansion chamber. The accuracy of *XFlow* results will be determined by comparing the numerical results with the experimental data of Selamet and Radavich [20] for the geometry described in Figure 5.1.

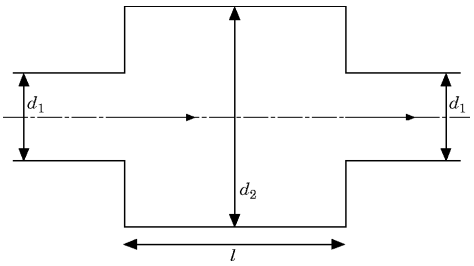

Parameter	Value
d_1	4.859 cm
d_2	15.318 cm
l	54 cm
l/d_2	3.525

Figure 5.1: Schematic of the muffler geometry

The transmission loss in such an expansion chamber is given by:

$$TL = 20log_{10}\frac{p_{inc}}{p_{tra}} \tag{5.1}$$

p_{inc} and p_{tra} being the incident and transmitted pressure respectively [21].

In this work, XFlow is used to find the ratio p_{inc}/p_{tra} and hence the transmission loss. The relevant parameters of the setup used to run the case are summarised in Table 5.1. Please note that the inlet boundary condition is a conditional function that sets a sinusoidal velocity of frequency 3200 Hz and an amplitude of 0.05 ms^{-1} and generates a pressure wave; the dissipation of which in the muffler is the object of this study.

Project tree parameter	Value
Engine	3D Single phase internal (Isothermal)
Acoustics analysis	On
Initial velocity field	(0 0 0) m s^{-1}
Initial gauge pressure	0 Pa
Reference area	Front
Reference velocity	Custom (0.05 ms^{-1})
Density [ρ]	1.225 kg m^{-3}
Dynamic viscosity [μ]	3.34e-5 Pa s
Enable bulk viscosity	On (3.34e-5 Pa s)
Muffler inlet - Velocity	if($t < 0.0003125$,$0.05 * sin(2 * pi * 3200 * t)$,0)
Muffler outlet - Gauge pressure outlet	0 Pa (Backflow: On)
Muffler shell - Wall	Free slip
Simulation time	0.035 s
Courant number	1
Resolved scale	0.0025 m
Refinement algorithm	Disabled

Table 5.1: Relevant simulation settings

Figure 5.2 shows the muffler numerical domain. In the figure, the position of two sensors is indicated - one at the muffler inlet and the other at the outlet. These sensors allow us to monitor the numerical value of p_{inc} and p_{tra}.

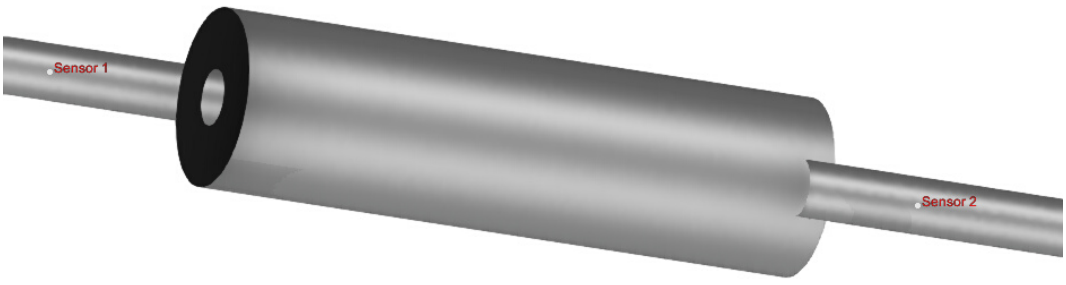

Figure 5.2: Muffler geometry showing the sensors position

Replacing the values of p_{inc} and p_{tra} into Equation (5.1), we obtain the transmission

loss predicted by *XFlow*. This is shown in Figure 5.3 together with the experimental data of Selamet and Radavich [20]. From the figure, it can be concluded that *XFlow* is able to accurately predict the acoustics behaviour of such a muffler.

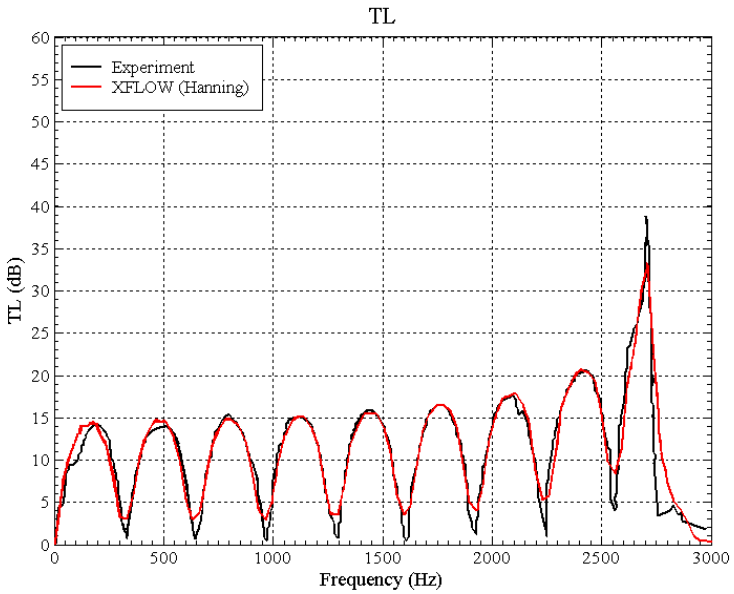

Figure 5.3: Transmission loss comparison between *XFlow* results and experimental data [20]

5.2 Helmholtz resonator: Flute

The sound generation in a small stopped flue pipe with recorder-like proportions was simulated using *XFlow*. The flute under study is similar to the one studied by Kühnelt in [22, 23]; its geometry is shown in Figure 5.4 and its relevant dimensions are reported in Table 5.2.

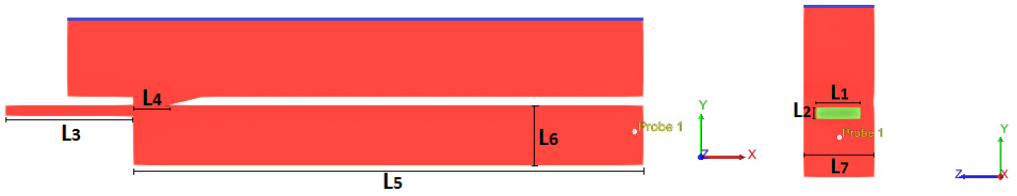

Figure 5.4: Flute geometry - Inlet in green and outlet in blue

Flute components	Nomenclature	Value
Inlet flue	$L_3 \times L_2 \times L_1$	$15 \times 4.5\times 1.2$ (mm)
Mouth opening length	L_4	3.75 (mm)
Resonant cavity	$L_5 \times L_6 \times L_7$	$60 \times 7 \times 7$ (mm)

Table 5.2: Geometry description

According to Helmholtz theory, the resonance frequency (f_H) of a cavity is given by:

$$f_H = \frac{c_s}{2\pi}\sqrt{\frac{A}{V_o L}} \tag{5.2}$$

where c_s is the speed of sound, A represents the cross-sectional area of the neck, L stands for the neck length and V_o is the cavity volume. In particular, from Table 5.2 we have: $A = 0.0012 * 0.0045\ m^2$, $L = 0.00375\ m$, $V_o = 0.007 * 0.007 * 0.06\ m^3$ and $c_s = 340\ m/s$; replacing the corresponding values into Eq. (5.2) it is found that the theoretical resonance-frequency of this flute is $1197 Hz$ [23].

This flute has been simulated with *XFlow* to validate its acoustic analysis (Acoustic analysis is available in Expert mode, `Preferences > Application > Application mode: Expert mode`). The case setup is summarised in Table 5.3 and the velocity contours inside the flute at $t = 0.01\ s$ and $t = 0.0106\ s$ are shown in Figure 5.5.

As indicated in Table 5.3, a `Probe` has been placed at the end of the resonant cavity to measure the static-pressure variation in time. This is shown in Figure 5.6. The compression-expansion cycles at the probe position are clearly observed in the figure. This information is further shown in Figure 5.7 in terms of Sound Pressure Level (SPL) versus frequency.

Project tree parameter	Value
Engine	3D Single phase internal (Isothermal)
Acoustics analysis	On
Initial velocity field	(0 0 0) m s^{-1}
Initial gauge pressure	0 Pa
Density [ρ]	1.205 kg m^{-3}
Dynamic viscosity [μ]	1.7894e-5 Pa s
Flute inlet - Velocity	7.76 ms^{-1}
Flute outlet - Gauge pressure outlet	0 Pa
Simulation time	0.02 s
Courant number	1
Resolved scale	0.00022 m
Refinement algorithm	Disabled
Probe position	(0.074, -0.003, 0) m

Table 5.3: Relevant simulation settings

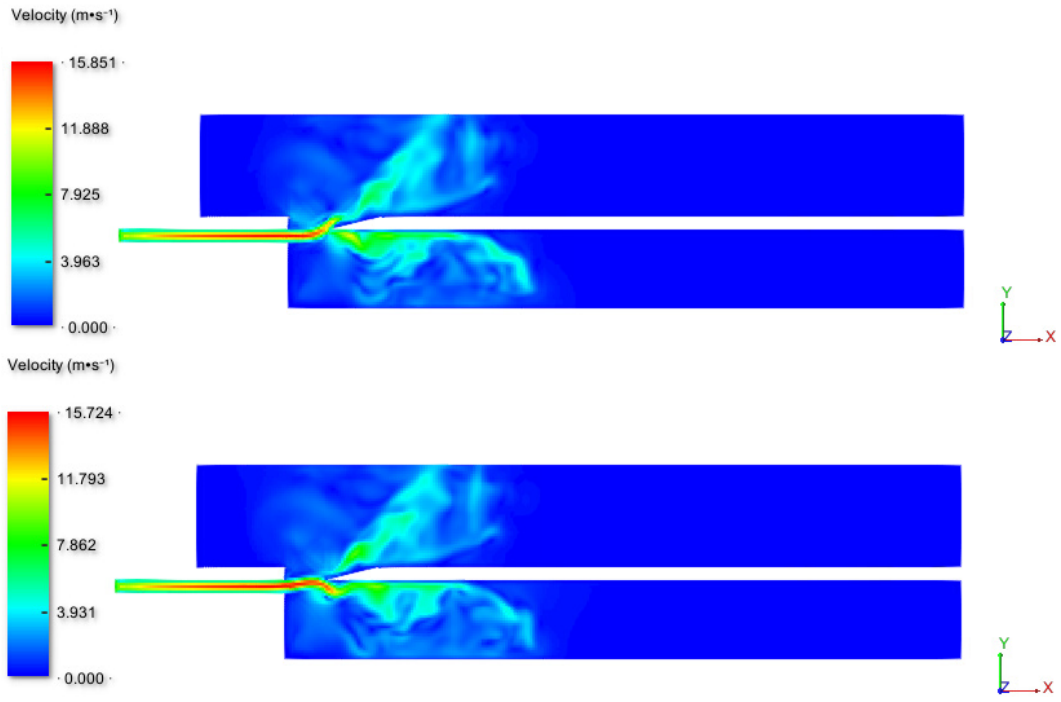

Figure 5.5: Velocity contours inside the flute at $t = 0.01$ s and $t = 0.0106$ s

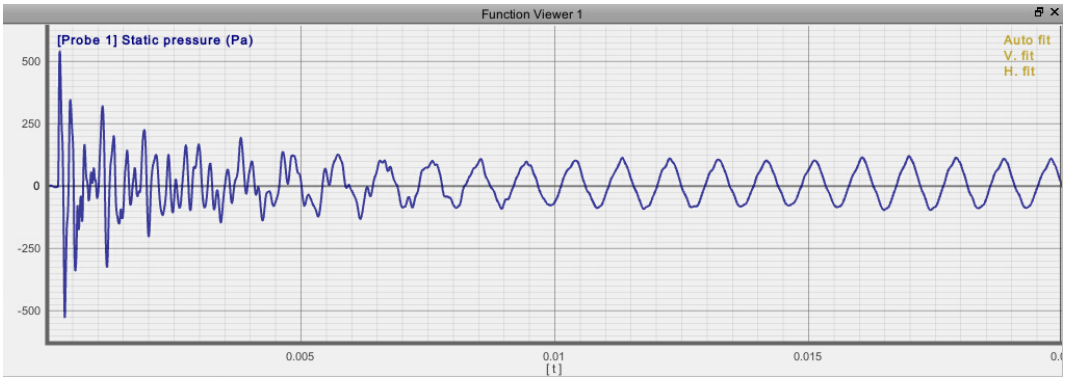

Figure 5.6: Helmholtz resonator - Static pressure measured at the probe position

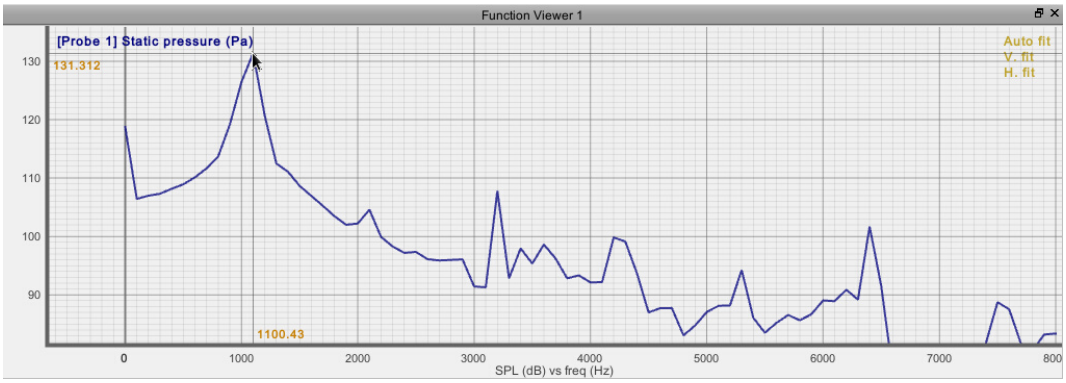

Figure 5.7: Helmholtz resonator - Sound pressure level vs frequency at the probe position

Figure 5.7 shows that the fundamental frequency of the cavity appears at about 1100 Hz which is in close agreement with 1197 Hz - the theoretical value predicted by Helmholtz formula.

6 Heat transfer

Contents

6.1 Natural convection in a cavity

Natural convection in a cavity is a classical test case for the modelling of buoyancy driven flows. A schematic of the problem is shown in Figure 6.1. It consists of a fluid enclosed in a square cavity with different wall temperatures. This leads to a thermal gradient that gives rise to the natural convection of the fluid. Horizontal walls are considered adiabatic.

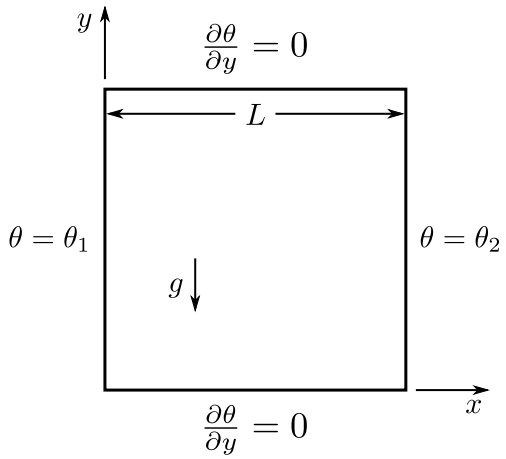

Figure 6.1: Geometry and boundary conditions.

XFlow models the buoyancy forces according to the Boussinesq approximation, that assumes the linear variation of the density as a function of the temperature θ:

$$\rho = \rho_0[1 - \alpha(\theta - \theta_0)]$$

and that the thermodynamic properties of incompressible fluids are constant except when considering the body force $\rho \boldsymbol{g}$ in the momentum equation. Hence, the governing equations of the fluid motion are as follows:

$$\text{Mass conservation:} \qquad \boldsymbol{\nabla} \cdot \boldsymbol{v} = 0 \tag{6.1}$$

$$\text{Momentum conservation:} \qquad \rho_0 \frac{\mathrm{d}\boldsymbol{v}}{\mathrm{d}t} = \boldsymbol{\nabla} \cdot \boldsymbol{\sigma} + \rho_0[1 - \alpha(\theta - \theta_0)]\boldsymbol{g} \tag{6.2}$$

$$\text{Enthalpy conservation:} \qquad \rho_0 c_p \frac{\mathrm{d}\theta}{\mathrm{d}t} = k\boldsymbol{\nabla} \cdot (\nabla\theta) + \Phi \tag{6.3}$$

where α is the thermal expansion coefficient, c_p the specific heat at constant pressure, k the thermal diffusion coefficient, θ_0 a reference temperature, $\rho_0 = \rho(\theta_0)$, and Φ is the viscous heat dissipation.

Benchmark solutions for this natural convection problem were published by de Vahl Davis [24]. These solutions are compared with the numerical results obtained with *XFlow* for several spatial resolutions (20x20, 40x40, 80x80, and 160x160 lattice points) and for two Rayleigh numbers ($Ra = 10^3,\ 10^6$):

$$Ra = \frac{\rho\, g\, \alpha\, \Delta\theta\, L^3}{\mu\, \kappa} \tag{6.4}$$

$\Delta\theta = |\theta_1 - \theta_2|$ being the temperature difference between the two vertical walls and $L = 1$ m being the cavity side length. The fluid properties for the first case ($Ra = 10^3$) are given in Table 6.1.

Case	$Ra = 10^3$	$Ra = 10^6$
ρ_0	1 kg m^{-3}	1 kg m^{-3}
g	-10 m s^{-2}	-10 m s^{-2}
α	0.1 K^{-1}	0.1 K^{-1}
$\Delta\theta$	1 K	1 K
μ	0.0266458 Pa s	0.0008426 Pa s
k	0.0375293 kg m s^{-3} K^{-1}	0.0011868 kg m s^{-3} K^{-1}
c_p	1 m^2 s^{-2} K^{-1}	1 m^2 s^{-2} K^{-1}

Table 6.1: Fluid properties

The values of μ, k and c_p are chosen to match the air Prandtl number: $Pr = \dfrac{\mu\, c_p}{k} = 0.71$. In both cases, the viscous heat dissipation has been neglected as it is done in [24].

The comparison is made in terms of the the following dimensionless variables at steady state:

$$X = \frac{x}{L}, \quad Y = \frac{y}{L}, \quad V_x = \frac{v_x L}{\kappa}, \qquad V_y = \frac{v_y L}{\kappa}, \quad \text{and} \quad \overline{Nu}_0 = \int_0^1 \frac{\partial\theta}{\partial x}\, dy \Big|_{X=0}$$

where $\kappa = \dfrac{k}{\rho\, c_p}$ is the thermal diffusivity of the fluid.

Tables 6.2 and 6.3 show the comparison of XFlow results with the solution in [24] for $Ra = 10^3$ and $Ra = 10^6$, where:

- $\overline{Nu}_0$, average heat flux in the hot vertical wall
- $\max V_x$, maximum value of the non-dimensional horizontal velocity on the vertical centreline and its location Y_{max}
- $\max V_y$, maximum value of the non-dimensional vertical velocity on the horizontal centreline and its location X_{max}

There is a good agreement in both cases although the accuracy decreases for the highest Rayleigh number. This is consistent with the findings of most contributors reported in [24]. In this test, the maximum and minimum locations are cell centered, none of the interpolation techniques suggested by [25] have been employed.

Velocity, vorticity and temperature contours resulting from the XFlow simulations are shown in Figures 6.2 and 6.3 for $Ra = 10^3$ and $Ra = 10^6$ respectively.

For this case it is essential to: (i) deactivate the viscous heat dissipation Φ (`Environment > Engine > Advanced Options > Enable viscous term in energy equation:` Off); (ii) do not use turbulence model (`Environment > Engine > Turbulence settings/ Turbulence generation:` Off); and (iii) set a unity Courant number(`Co` $\approx$ 1), as large Courant values would introduce an excessive compressibility in the flow and the results will not correspond to the Boussinesq incompressible reference solution.

	20x20	40x40	80x80	160x160	Ref.[24]
max V_x	3.5428	3.6325	3.6422	3.6468	3.649
at Y_{max}	0.825	0.8125	0.8187	0.8156	0.813
max V_y	3.6359	3.6941	3.7023	3.7012	3.697
at X_{max}	0.175	0.1875	0.1812	0.1781	0.178
$\overline{Nu}_0$	1.0916	1.1072	1.1129	1.1155	1.117

Table 6.2: Case $Ra = 10^3$. Comparison of *XFlow* results with the solution in [25] for different spatial resolutions.

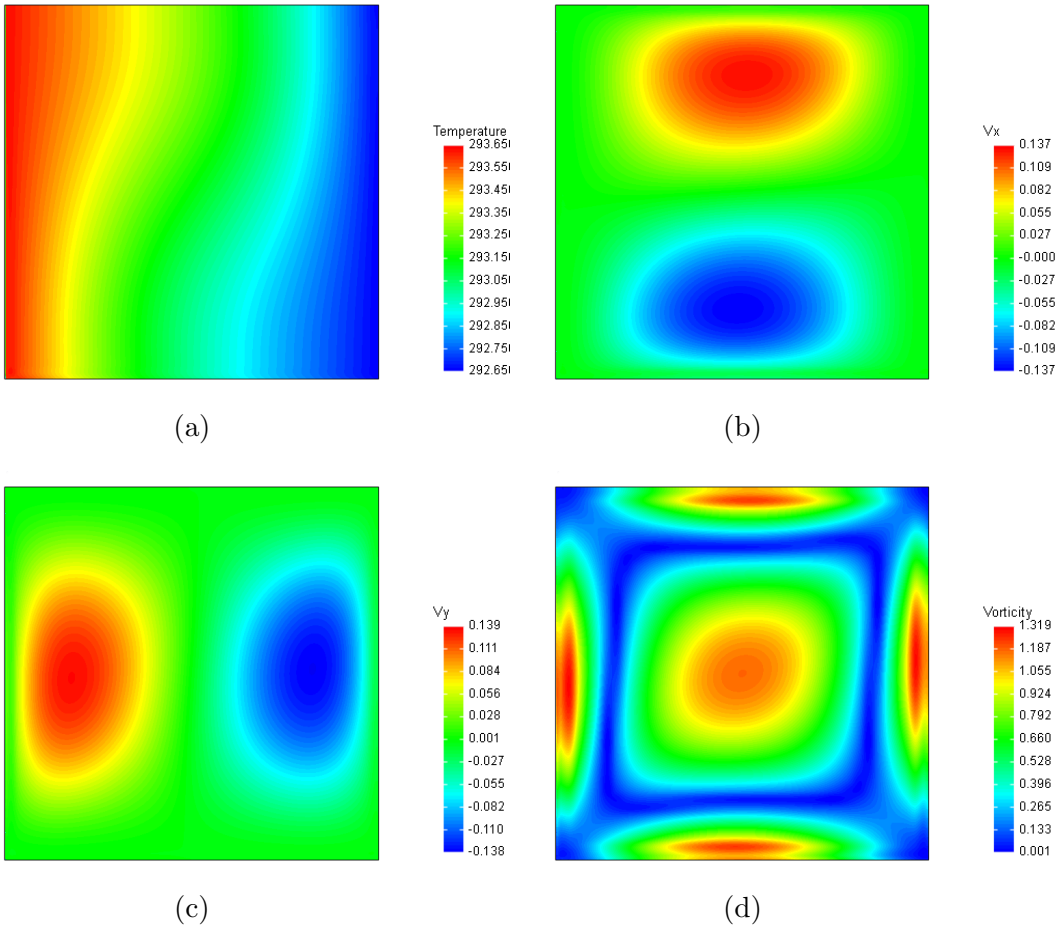

Figure 6.2: Result fields for $Ra = 10^3$: (a) temperature, (b) horizontal velocity, (c) vertical velocity, and (d) vorticity.

	20x20	40x40	80x80	160x160	Ref.[24]
$\max V_x$	54.448	57.750	63.805	64.902	64.630
at Y_{max}	0.875	0.863	0.856	0.847	0.850
$\max V_y$	127.259	193.479	215.178	219.817	219.360
at X_{max}	0.075	0.038	0.044	0.041	0.038
$\overline{Nu}_0$	5.924	7.975	8.688	8.823	8.817

Table 6.3: Case $Ra = 10^6$. Comparison of *XFlow* results with the solution in [25] for different spatial resolutions.

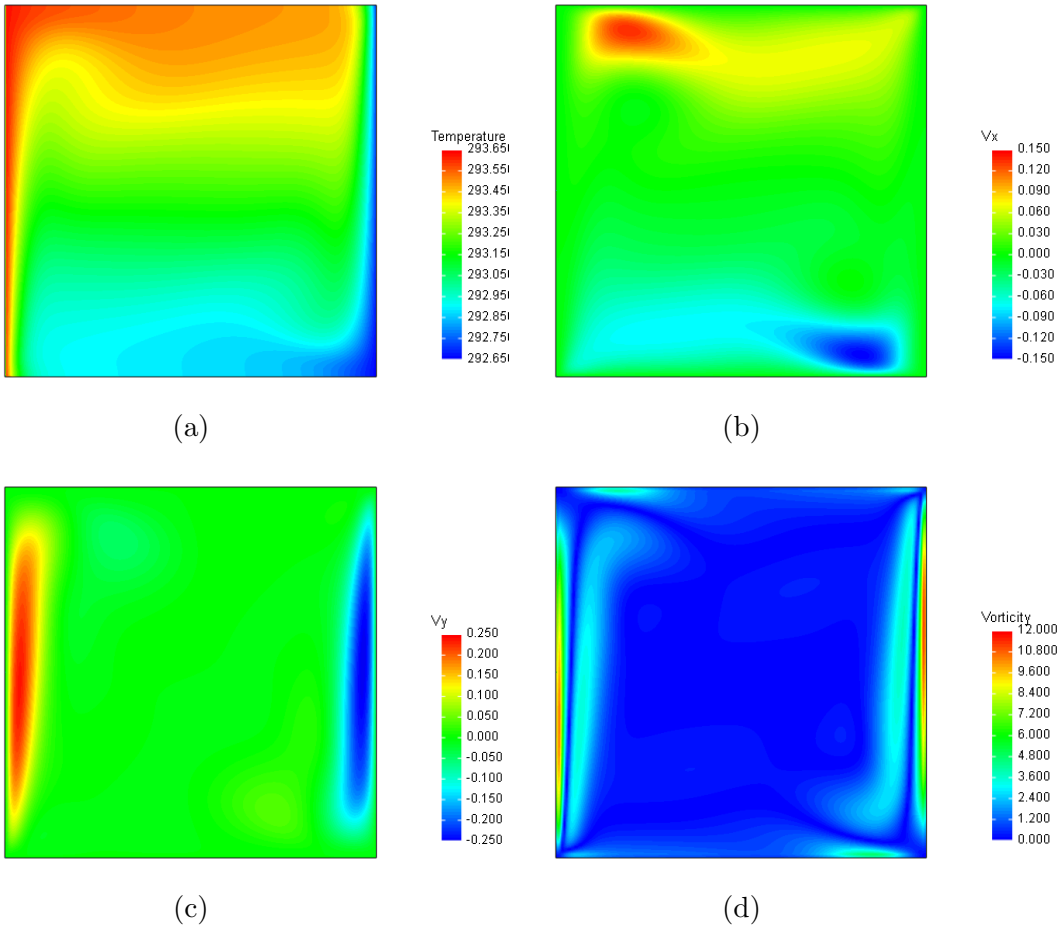

(a) (b)

(c) (d)

Figure 6.3: Result fields for $Ra = 10^6$: (a) temperature, (b) horizontal velocity, (c) vertical velocity, and (d) vorticity.

7

Multi-phase flows

Contents

7.1 Rayleigh-Taylor

When heavy fluid lies above lighter, the equilibrium in unstable and a small perturbation of the interface from the horizontal will grow with time, producing the phenomenon known as Rayleigh-Taylor instability [26]. This instability is a prototype problem for computational studies of multi-phase flows.

The problem consists of two layers of fluid initially at rest in the rectangular domain $\Omega = (-d/2, d/2) \times (-2d, 2d)$, see Figure 7.1. The flow is characterized by the density difference between the two fluids and their effective viscosity.

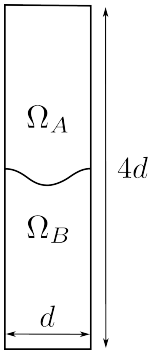

d	1	m
ρ_A	3000	kg/m^3
ρ_B	1000	kg/m^3
μ_A	1	Pa s
μ_B	1	Pa s
g	1	m/s^2

Figure 7.1: Initial configuration and physical properties of the fluids.

The density difference is represented by the Atwood number $At = (\rho_A - \rho_B)/(\rho_A + \rho_B)$. The Reynolds number is defined as $Re = \rho_A\, d^{3/2}\, g^{1/2}/\mu$, where d is the reference length, g the gravity acceleration and μ the dynamic viscosity of the fluids (assumed uniform).

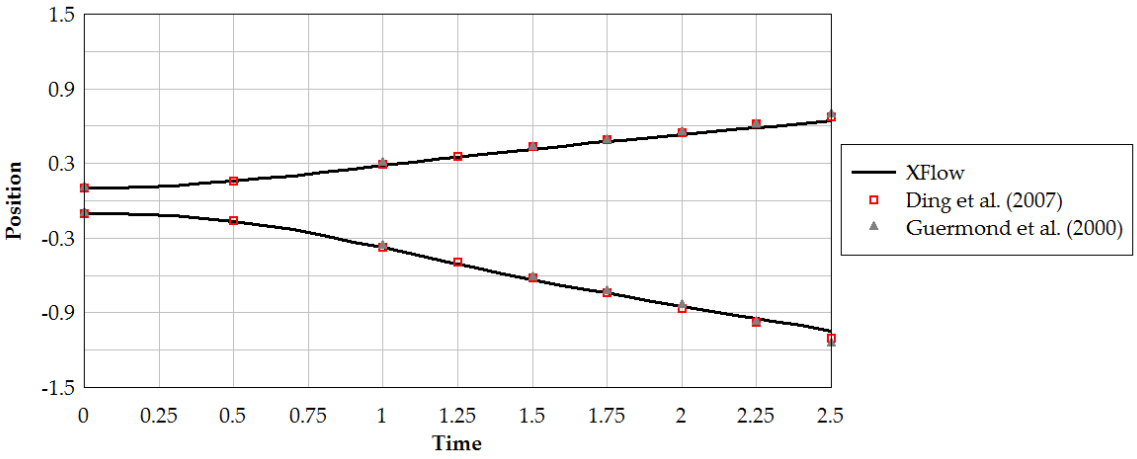

Figure 7.2: Vertical position of spike and bubble vs. time. Comparison of *XFlow* solution with reference ones.

The growth and evolution of Rayleigh–Taylor instability has been investigated among others by Tryggvason [27] for inviscid incompressible flows, and by Guermond & Quartapelle [28] and Ding et al. [29] for viscous flows. None of these studies has taken into account surface tension.

We compare the *XFlow* results with those of [28] and [29] at $At = 0.5$ and $Re = 3000$. The initial position of the perturbed interface is $y(x) = -0.1\, d \cos(2\pi x/d)$. Computations are carried out on a 200×800 grid and the time step is automatically set to 0.000144 s. Free-slip condition is enforced at all walls. The tracking of the interface is done using the marker-and-cell method.

Results on the vertical position of the tip of the falling and rising fluid (spike and bubble, respectively) are shown in Figure 7.2. *XFlow* solution is in good agreement with the reference results [28, 29].

The evolution of the instability is shown in Figure 7.3 at dimensionless times $\tilde{t}$ =0, 1, 1.25, 1.5, 1.75, 2, 2.25, 2.5, where $\tilde{t} = t\sqrt{g\,At}$. Around $\tilde{t} = 1.5$ the heavy fluid begins to roll up into two counter-rotating vortices (see also Figure 7.4). Later, around $\tilde{t} = 2$, these two vortices become unstable and a pair of secondary vortices appear at the tails of the roll-ups. The roll-ups and vortices in the heavy fluid spike are due to the Kelvin–Helmholtz instability. The shapes of the fluid interface obtained with *XFlow* compare well with those of the reference results [28, 29].

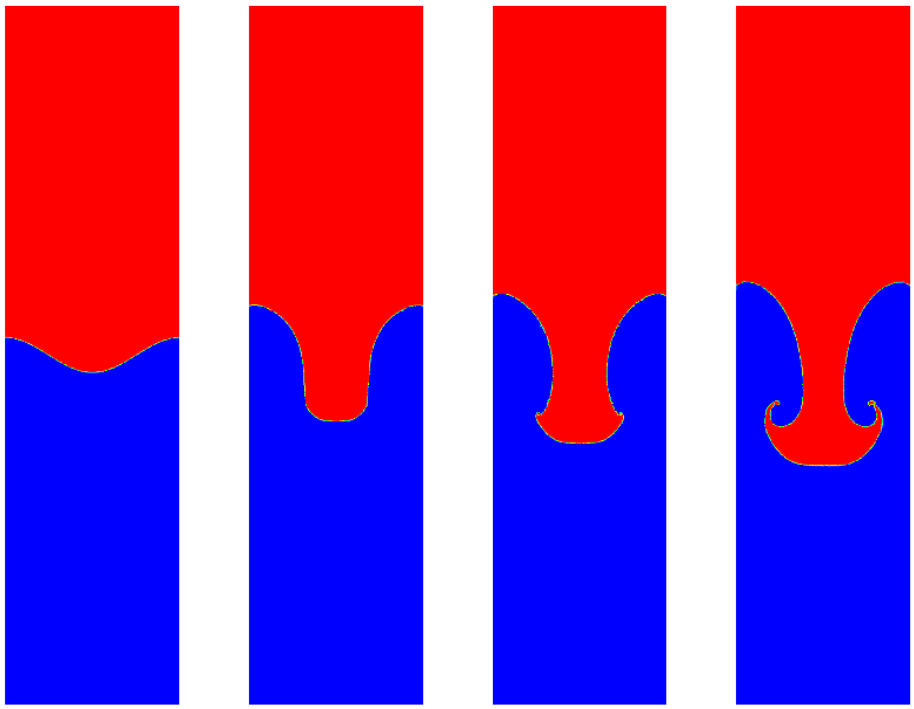

$\tilde{t} = 0$ $\tilde{t} = 1$ $\tilde{t} = 1.25$ $\tilde{t} = 1.5$

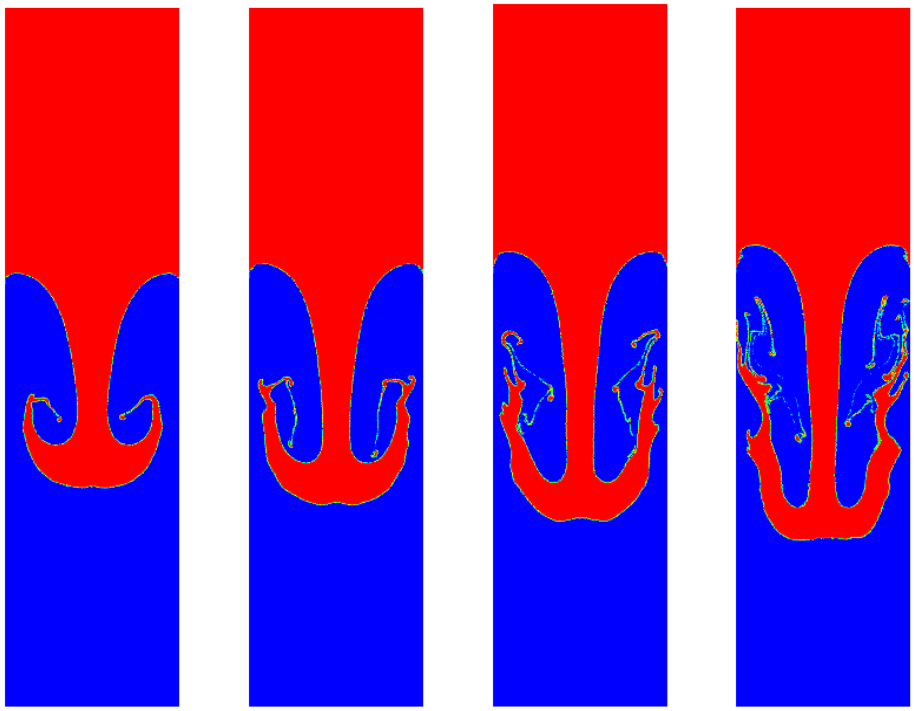

$\tilde{t} = 1.75$ $\tilde{t} = 2$ $\tilde{t} = 2.25$ $\tilde{t} = 2.5$

Figure 7.3: Rayleigh-Taylor instability evolution.

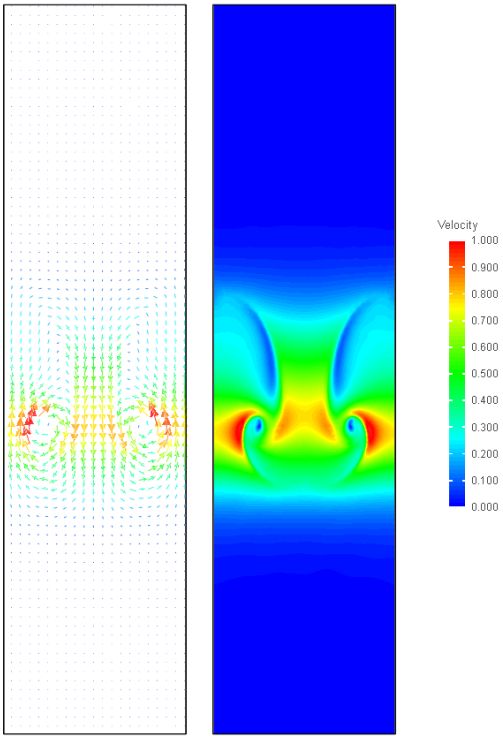

Figure 7.4: Velocity field at $\tilde{t} = 1.5$ s.

References

[1] C.-H. Bruneau and M. Saad. The 2d lid-driven cavity problem revisited. *Computers & Fluids*, 35:326–348, 2006.

[2] U. Ghia, K.N. Ghia, and C.T. Shin. High-Re solutions for incompressible flow using the Navier-Stokes equations and a multigrid method. *Journal of Computational Physics*, 48:387–411, 1982.

[3] Wim M Van Rees, Anthony Leonard, DI Pullin, and Petros Koumoutsakos. A comparison of vortex and pseudo-spectral methods for the simulation of periodic vortical flows at high reynolds numbers. *Journal of Computational Physics*, 230(8):2794–2805, 2011.

[4] C. Rumsey, R. Biedron, and J. Thomas. CFL3D: Its history and some recent applications. Technical report, NASA TM-112861, 1997.

[5] D.P. Lockard, L.-S. Luo, S.D. Milder, and B.A. Singer. Evaluation of PowerFLOW for Aerodynamic Applications. *Journal of Statistical Physics*, 107(1/2):423–478, 2002.

[6] D. Somers. Design and experimental results for the s825 airfoil. Technical report, National Renewable Energy Laboratory, 2005.

[7] R. J. McGhee, W. D. Beasley, and J. M. Foster. Recent modifications and calibration of the langley low-turbulence pressure tunnel. Technical report, NASA TP-2328, 1984.

[8] P. A. Baranov, S. V. Guvernyuk, M. A. Zubin, and S. A. Isaev. Numerical and physical modeling of the circulation in a vortex cell in the wall of a rectilinear channel. *Fluid Dynamics*, 35:663–673, 2000.

[9] S.A. Isaev, S.V. Guvernyuk, M.A. Zubin, and Y.S. Prigorodov. Numerical and physical modeling of a low-velocity air flow in a channel with a circular vortex cell. *Journal of Engineering Physics and Thermophysics*, 73:337–344, 2000.

[10] R. Donelli, P. Iannelli, S. Chernyshenko, A. Iollo, and L. Zannetti. Flow models for a vortex cell. *AIAA Journal*, 47:451–467, 2009.

[11] C. Rumsey. The 1st AIAA CFD High Lift Prediction Workshop (HiLiftPW-1), NASA Langley Research Center, http://hiliftpw.larc.nasa.gov/index-workshop1.html.

[12] C.B. Mc Ginley, L.N. Jinkins, R.D. Watson, and A. Bertelrud. 3-D High-Lift Flow-Physics Experiment - Transition Measurements. *AIAA Paper*, 2005-5148, 2005.

[13] G. Le Good and K. Garry. On the use of reference models in automotive aerodynamics. *SAE paper*, 2004-01-1308.

[14] S.R. Ahmed and G. Ramm. Some Salient Features of the Time-Averaged Ground Vehicle Wake. *SAE-Paper 840300*, 1984.

[15] C. Hinterberger, M. García-Villalba, and W. Rodi. *Large eddy simulation of flow around the Ahmed body*, pages 77–87. Springer Berlin Heidelberg, Berlin, Heidelberg, 2004.

[16] G. Franck, N. Nigro, M. A. Storti, and J. D'Elia. Numerical simulation of the flow around the Ahmed vehicle model. *Latin American applied research*, 39:295–295, 2009.

[17] B. Metcalf, J. Longo, S. Ghosh, and F. Stern. Unsteady free-surface wave-induced boundary-layer separation for a surface-piercing NACA 0024 foil: Towing tank experiments. *Journal of Fluids and Structures*, 22:77–98, 2006.

[18] K.M.T. Kleefsman, G. Fekken, A.E.P. Veldman, B. Iwanowski, and B. Buchner. A Volume-of-Fluid based simulation method for wave impact problems. *Journal of Computational Physics*, 206:363–393, 2005.

[19] J. J. Stoker. *Water Waves; The Mathematical Theory with Applications*. 1992.

[20] A. Selamet and P.M. Radavich. The effect of length on the acoustic attenuation performance of concentric expansion chambers: An analytical, computational and experimental investigation. *Journal of Sound and Vibration*, 201(4):407–426, 1997.

[21] J. M. Middelberg, T. J. Barber, S. S. Leong, K.P. Byrne, and E. Leonardi. Computational fluid dynamics analysis of the acoustic performance of various

simple expansion chamber mufflers. *Proceedings of ACOUSTICS,*, pages 123–128, 3-5 November 2004, Gold Coast, Australia.

[22] Helmut Kï¿½hnelt. Simulating the mechanism of sound generation in flutes using the lattice Boltzmann method. *Proceedings of the Stockholm Music Acoustics Conference*, pages SMAC–1 – SMAC–4, August 6-9 2003, Stockholm Sweden.

[23] W. Kausel and H. Kï¿½hnelt. Modelling wave and fluid propagation in wind instruments. *Methods and Applications.*

[24] G. DeVahl Davis and I.P. Jones. Natural convection in a square cavity: a comparison exercise. *International Journal for Numerical Methods in Fluids*, 3:227–248, 1983.

[25] G. de Vahl Davis. Natural convection of air in a square cavity: a benchmark numerical solution. *International Journal for Numerical Methods in Fluids*, 3:249–264, 1983.

[26] D.H. Sharp. An overview of Rayleigh-Taylor instability. *Physica D*, 12:3–18, 1984.

[27] G. Tryggvason. Numerical simulations of the Rayleigh-Taylor instability. *Journal of Computational Physics*, 75:253–282, 1988.

[28] J.-L. Guermond and L. Quartapelle. A projection FEM for variable density incompressible flows. *Journal of Computational Physics*, 165:167ï¿½188, 2000.

[29] H. Ding, P. Spelt, and C. Shu. Diffuse interface model for incompressible two-phase flows with large density ratios. *Journal of Computational Physics*, 226:2078ï¿½2095, 2007.

Our **3D**EXPERIENCE® platform powers our brand applications, serving 11 industries, and provides a rich portfolio of industry solution experiences.

Dassault Systèmes, the **3D**EXPERIENCE Company, is a catalyst for human progress. We provide business and people with collaborative virtual environments to imagine sustainable innovations. By creating 'virtual experience twins' of the real world with our **3D**EXPERIENCE platform and applications, our customers push the boundaries of innovation, learning and production.

Dassault Systèmes' 20,000 employees are bringing value to more than 270,000 customers of all sizes, in all industries, in more than 140 countries. For more information, visit **www.3ds.com**.

DASSAULT SYSTEMES | The **3D**EXPERIENCE® Company

Americas
Dassault Systèmes
175 Wyman Street
Waltham, Massachusetts
02451-1223
USA

Europe/Middle East/Africa
Dassault Systèmes
10, rue Marcel Dassault
CS 40501
78946 Vélizy-Villacoublay Cedex
France

Asia-Pacific
Dassault Systèmes K.K.
ThinkPark Tower
2-1-1 Osaki, Shinagawa-ku,
Tokyo 141-6020
Japan